

AD \_\_\_\_\_

GRANT NUMBER DAMD17-98-1-8121

TITLE: Ultrasonic Stimulated Acoustic Emission for Detection of  
Breast Microcalcifications

PRINCIPAL INVESTIGATOR: Mostafa Fatemi, Ph.D.

CONTRACTING ORGANIZATION: Mayo Foundation  
Rochester, Minnesota 55905

REPORT DATE: May 1999

TYPE OF REPORT: Annual

PREPARED FOR:  
U.S. Army Medical Research and Materiel Command  
Fort Detrick, Maryland 21702-5012

DISTRIBUTION STATEMENT: Approved for Public Release;  
Distribution Unlimited

The views, opinions and/or findings contained in this report are those of the author(s) and should not be construed as an official Department of the Army position, policy or decision unless so designated by other documentation.

20000828 114

| REPORT DOCUMENTATION PAGE   |  |   | Form Approved<br>OMB No. 0704-0188                  |  |
|---|--|---|---|--|
| <small>Public reporting burden for this collection of information is estimated to average 1 hour per response, including the time for reviewing instructions, searching existing data sources, gathering and maintaining the data needed, and completing and reviewing the collection of information. Send comments regarding this burden estimate or any other aspect of this collection of information, including suggestions for reducing this burden, to Washington Headquarters Services, Directorate for Information Operations and Reports, 1215 Jefferson Davis Highway, Suite 1204, Arlington, VA 22202-4302, and to the Office of Management and Budget, Paperwork Reduction Project (0704-0188), Washington, DC 20503.</small>   |  |   |   |  |
| 1. AGENCY USE ONLY (Leave blank)  |  | 2. REPORT DATE<br>May 1999                              |   | 3. REPORT TYPE AND DATES COVERED<br>Annual (15 Apr 98 - 14 Apr 99) |
| 4. TITLE AND SUBTITLE<br>Ultrasonic Stimulated Acoustic Emission for Detection of Breast Microcalcifications  |  |   | 5. FUNDING NUMBERS<br>DAMD17-98-1-8121              |  |
| 6. AUTHOR(S)<br>Mostafa Fatemi, Ph.D.   |  |   |   |  |
| 7. PERFORMING ORGANIZATION NAME(S) AND ADDRESS(ES)<br>Mayo Foundation<br>Rochester, Minnesota 55905   |  |   | 8. PERFORMING ORGANIZATION<br>REPORT NUMBER         |  |
| 9. SPONSORING / MONITORING AGENCY NAME(S) AND ADDRESS(ES)<br>U.S. Army Medical Research and Materiel Command<br>Fort Detrick, Maryland 21702-5012   |  |   | 10. SPONSORING / MONITORING<br>AGENCY REPORT NUMBER |  |
| 11. SUPPLEMENTARY NOTES   |  |   |   |  |
| 12a. DISTRIBUTION / AVAILABILITY STATEMENT<br>Approved for Public Release; Distribution Unlimited   |  |   | 12b. DISTRIBUTION CODE                              |  |
| 13. ABSTRACT (Maximum 200 words)<br><p>The <b>purpose</b> of this research is to build an experimental system based on Ultrasound Stimulated Acoustic Emission for <i>in vitro</i> imaging of breast tissue specimens, with the goal of detecting microcalcifications with sufficient accuracy. The <b>scope</b> of this research is to develop a laboratory system and evaluate its performance on phantoms and specimens of human breast tissues containing microcalcifications. The first task of this research, which covers the first year and a part of the second year, focuses on system development and optimization for detection of breast microcalcification. This task includes the development of both the theoretical model and experimental setup required for the method. Our <b>findings</b> include the development of the fundamental theory that describes the relationship between the incident ultrasonic wave and the resulting acoustic emission field in terms of the mechanical parameters of the object. This theory also describes the point spread function, from which we can determine the theoretical spatial resolution of the system. We have also improved our experimental system, by substantially reducing the acoustic noise and minimizing the multipath effect, both critical in reliable detection of microcalcifications in breast tissue. We are now able to detect 260-<math>\mu</math>m-diameter glass beads in gel.</p> |  |   |   |  |
| 14. SUBJECT TERMS<br>Breast Cancer  |  |   | 15. NUMBER OF PAGES<br>58                           |  |
|   |  |   | 16. PRICE CODE                                      |  |
| 17. SECURITY CLASSIFICATION OF REPORT<br>Unclassified   | 18. SECURITY CLASSIFICATION OF THIS PAGE<br>Unclassified | 19. SECURITY CLASSIFICATION OF ABSTRACT<br>Unclassified | 20. LIMITATION OF ABSTRACT<br>Unlimited             |  |

## FOREWORD

Opinions, interpretations, conclusions and recommendations are those of the author and are not necessarily endorsed by the U.S. Army.

\_\_\_\_ Where copyrighted material is quoted, permission has been obtained to use such material.

\_\_\_\_ Where material from documents designated for limited distribution is quoted, permission has been obtained to use the material.

MF Citations of commercial organizations and trade names in this report do not constitute an official Department of Army endorsement or approval of the products or services of these organizations.

\_\_\_\_ In conducting research using animals, the investigator(s) adhered to the "Guide for the Care and Use of Laboratory Animals," prepared by the Committee on Care and use of Laboratory Animals of the Institute of Laboratory Resources, national Research Council (NIH Publication No. 86-23, Revised 1985).

\_\_\_\_ For the protection of human subjects, the investigator(s) adhered to policies of applicable Federal Law 45 CFR 46.

\_\_\_\_ In conducting research utilizing recombinant DNA technology, the investigator(s) adhered to current guidelines promulgated by the National Institutes of Health.

\_\_\_\_ In the conduct of research utilizing recombinant DNA, the investigator(s) adhered to the NIH Guidelines for Research Involving Recombinant DNA Molecules.

\_\_\_\_ In the conduct of research involving hazardous organisms, the investigator(s) adhered to the CDC-NIH Guide for Biosafety in Microbiological and Biomedical Laboratories.

M. J. Fatemi 5/4/99  
PI - Signature Date

## TABLE OF CONTENTS

|   |       |
|---|-------|
| <u>Front Cover</u> . . . . .  | 1     |
| <u>Letter Indicating No Proprietary or Unpublished Data</u> . . . . . | 2     |
| <u>Report Documentation Page</u> . . . . .                            | 3     |
| <u>Foreword</u> . . . . .   | 4     |
| <u>Table of Contents</u> . . . . .                                    | 5     |
| <u>Introduction</u> . . . . .   | 6     |
| <u>Body</u> . . . . .   | 6-18  |
| <u>Key Research Accomplishments</u> . . . . .                         | 18    |
| <u>Reportable Outcomes</u> . . . . .                                  | 18-19 |
| <u>Conclusions</u> . . . . .  | 19    |
| <u>References</u> . . . . .   | 19-20 |
| <u>Appendices</u> . . . . .   | 20-59 |

Appendix A: Figures and legends (pages 21-23 of this report)

Appendix B: Fatemi, M., and J. F. Greenleaf: Ultrasound-stimulated vibro-acoustic spectrography. Science 280:82-85, April 3, 1998 (pages 24-27 of this report)

Appendix C: Fatemi, M., and J. F. Greenleaf: Vibro-acoustography: An imaging modality based on ultrasound-stimulated acoustic emission. Proceedings of the National Academy of Sciences USA (In Press) (see pages 28-56 of this report)

Appendix D: Fatemi, M., and J. F. Greenleaf: Acoustic field calculation in ultrasound-stimulated vibro-acoustography. Second International Conference on Ultrasound in Medicine and Engineering, Beijing, China, August 26-28, 1998 (Abstract) (see page 57 of this report)

Appendix E: Fatemi, M., and J. F. Greenleaf: Potential applications of ultrasound-stimulated vibro-acoustography in medical diagnosis and material characterization. 137th Meeting of the Acoustical Society of America and 2nd Convention of the European Acoustical Association, Berlin, Germany, March 14-19, 1999 (Invited Abstract) (page 58 of this report)

Appendix F: Fatemi, M., and J. F. Greenleaf: Beam forming for ultrasound-stimulated vibro-acoustography. ICTCA/99 Fourth International Conference on Theoretical and Computational Acoustics, Trieste, Italy, May 10-14, 1999 (Keynote presentation) (page 59 of this report)



## 1 INTRODUCTION

Currently, x-ray mammography is the only imaging modality used in clinics for detection of microcalcifications. This important tool, however, is ionizing and its sensitivity is greatly reduced in dense breasts. The vision of this research is to develop a non invasive ultrasound-acoustic method that can detect microcalcification in breast with sufficient accuracy. The general goal of this research is to build an experimental system based on Ultrasound Stimulated Acoustic Emission (USAE) for *in vitro* imaging of breast tissue specimens and test its performance in detecting microcalcification. The first task of this research, which covers the first year and a part of the second year, focuses on system development and optimization for detection of breast microcalcification. This task includes the development of both the theoretical model and experimental setup required for the method. This report addresses the activities performed in the first year in both areas. In particular, the report includes the development of the theoretical model representing the relationship between the incident ultrasonic wave and the resulting acoustic emission field, improvement of the laboratory setup to reduce the acoustic noise interference, and improvement of the scanning system.

## 2 BODY

In this section we describe research accomplishments associated with task 1. This task focuses on two general areas: (1) Theory and model development; (2) System improvement. Both areas have been addressed here. In our work on system improvement we often refer to some physical phenomena and their effect of image quality. These phenomena are briefly described in the following table. Later we will present the methods we have used to counter the unwanted effects of these phenomena on images.

Table 1 Major problems in the experimental setup of USAE system

| Cause                                   | Effects on image                                  |
|---|---|
| Ultrasound standing wave effect         | Contrast dependency on object-transducer distance |
| Acoustic noise                          | Limited image contrast, low detectability         |
| Mutiple reflection of acoustic emission | Contrast dependency on water level in the tank    |
| Multipath                               | False shades                                      |

### 2.a Transducer Design

#### 2.a.1) High-frequency Transducer

We have designed a 9 MHz confocal transducer. This transducer should provide better spatial resolution (about 200 microns) than our 3 MHz transducer. This transducer is under construction.

### 2.a.2) Composite Transducer

In order to detect small objects in a viscoelastic background, we need to reduce the background noise in the medium (water tank in our experiments). We have found that one such noise source is the acoustic field resulting from the vibration of the transducer case at the acoustic emission frequency  $\Delta\omega$ . The confocal transducer used in our experiments is comprised of a center disc element and an outer ring both constructed on a single piezoelectric ceramic cap. A possible source of the vibration is coupling between the elements. An alternative piezoelectric material that could be used for a transducer with lower inter-element coupling is a piezoelectric composite material. Based on this strategy, we designed and constructed a confocal composite transducer, with the center frequency, diameter, and focal length of 3.5 MHz, 25 mm, and 7 cm, respectively. The new transducer, although less noisy, unfortunately cannot be used at the same power level as the ceramic transducer because of its limited ability to dissipate heat.

### 2.a.3) Annular Array Design

We have noted that when we use a confocal transducer to focus two CW ultrasound beams on an object with a high reflection coefficient, the ultrasound beam reflects back and forth between the transducer and the object, producing a standing wave pattern. Multiple reflections can be strong because the object is located at the focal point of the concave transducer, allowing not only the incident beam, but all the multiple reflected beams to be focused on the object. Because of the standing wave effect, the acoustic emission field of the object becomes excessively dependent on the distance between the object and transducer.

To reduce the standing wave effect we have designed a multi-element planar annular array transducer. The elements are divided into two groups to produce a center beam and an outer beam similar to those of our conventional (concave) two-element confocal transducer. Here the focusing is achieved by introducing the proper phase to the elements of the array in each group. Hence in transmit mode, the transducer operates similar to our conventional two-element confocal transducer. However, in response to the reflected beam from the object, the transducer acts as a *planar* reflector to bounce the reflected beam back toward the object. This field (which is now reflected once by the object and once by the transducer) is divergent. Hence, multiple reflections rapidly lose their strength as they reflect back and forth between the object and the transducer.

### 2.a.4) New Accelerometer

When imaging small objects (such as a glass bead or microcalcification) in a viscoelastic background, the acoustic emission amplitude can be small. Detection of this field by a hydrophone would not be too difficult if the frequency is high. At low frequencies however, hydrophone sensitivity usually drops to a level that may not be sufficient for detection of such small particles. As an alternative detector, we have used an accelerometer. The new accelerometer (B&K, Model 4387) has a useful frequency range from 0.1 Hz to 8 kHz, with a sensitivity of 26 mv/ms<sup>-2</sup>. It can be placed directly in contact with the object to detect small vibrations. A potential application for the accelerometer is detection of the resonance frequency of the particles.

## **2.b Phantom Design**

To test the performance of the system we designed three phantoms.

Phantom 1 is made from RTV (Room Temperature Vulcanizing) material and includes an embedded glass bead. RTV is a rubber-like material with a density and sound velocity close to those of soft tissues. It is, however, stiffer than most soft tissues. The attenuation coefficient of this material is higher than most soft tissues. The glass bead with a diameter of 400  $\mu\text{m}$  is placed at a depth of 3 mm from the surface. The glass bead has a high acoustic impedance similar to that of breast microcalcifications.

Phantom 2 is also made from RTV, but it includes two 2-mm-diameter holes instead of the glass bead. The holes in this phantom are partially air filled, representing an object with very low acoustic impedance. Locations of the holes are 3 mm and 10 mm from the surface.

Phantom 3 is made from soft gel with some embedded glass beads at a depth of 10 mm. The density and the sound speed of the gel material is very close to that of soft tissue, and its stiffness is similar or lower than many soft tissues. This material has an attenuation coefficient much lower than that of soft tissue.

## **2.c Acoustic and Vibrational Noise Reduction in the Experimental System**

### **2.c.1) *Quiet Room***

The quiet room is built within the Ultrasound Research Laboratory, with no window to the outside. Its area is 3x3 meters. To reduce transmission of the noise from other rooms, the wall and the ceiling is covered by 2 in thick Sonex acoustical foam. The foam has a corrugated wavy surface reducing reflection of sound. The room hosts the air table and the scanning tank with a minimum of electronic equipment. The computer and other electronic instruments that have fans and produce a high level of audio noise are placed outside the quiet room while connected via cables that pass through the wall. The ambient airborne audio range noise in the quiet room measures approximately 20 dB less than the ambient noise level in the adjacent laboratory.

### **2.c.2) *Air Table***

To reduce transmission of structural vibrations to the experiment setup, an air table (Technical Manufacturing Corp., Model 68-571) is now used to support the water tank in which the experiments take place. This air table provides vertical isolation efficiency of 90-99% at 10 Hz.

### **2.c.3) *Reducing the Multipath and Reverberation Effects— New Tank Design and Absorbers***

Major problems that led us to design a new water tank for our experiments are described below (also briefly mentioned in Table 1):

Multipath problem — The acoustic emission field produced as a result of object vibration in a conventional water tank can travel along many paths before reaching the hydrophone. These field components can interact constructively or destructively depending on the path lengths. This phenomenon causes an error in the resulting image because the amplitude of the recorded acoustic emission changes with respect to the position of the object in the tank.

Reverberation problem — When the acoustic emission field travels back and forth between two parallel reflective surfaces of the tank, the acoustic field may reach a resonance state, in which the field amplitude would become highly dependent on the wavelength and the tank size. This phenomenon can particularly be a problem when the sound reverberates between the water surface and the bottom of the tank, causing the acoustic amplitude to vary with the slightest ripple on the water surface.

New tank design — To reduce both the multipath and reverberation problems a new tank was designed and constructed. The new tank has a double layer bottom with the top layer positioned in a 15 degree angle with respect to the lower layer. The interior of the tank is covered with sound absorbing material (Sorbothane, Sorbothane Inc.). This material is highly absorbent, reducing the multipath and reverberation effects in the tank. The angled bottom also reduces the possibility of reverberation between the water surface and the tank bottom.

## **2.d Improving the Scanning and Data Acquisition Hardware and Software to Increase the Scanning Speed and Decreasing the Acoustic Noise of the Scanning Mechanism**

Slow scanning speed problem — Because our imaging method operates on one point of the object at a time, the process can take a long time. In addition, due to the mechanical vibration of the scanning mechanism, the scanner needs a period of time (usually a fraction of a second) to settle after it moves to a new point. This time plus the time required to acquire and transfer the data to the disk can be substantial.

### *2.d.1) High-speed Scanning*

In order to speed up the scanning process, we must prevent the noise and vibrations caused by the scanning structure from interfering with the acoustic emission data. One way to do this is by increasing the acoustic emission frequency beyond the spectral bandwidth of the scanner generated noise, such that the noise can be filtered out without losing the acoustic emission signal.

Based on this strategy, we have performed high-speed scanning at 30–60 kHz. A programmable filter was used to remove the scanner noise. The noise bandwidth in our system is about 20 kHz. In this method, the transmitting transducer continuously transmits the ultrasound while the scanner scans the object without stopping, and at the same time the hydrophone continuously receives the resulting acoustic emission signal. Using this method an object can be scanned in a fraction of the time that would be required for scanning by the conventional point-by-point scanning. The resulting images have high signal-to-noise ratio. The only drawback of this method is that it can not be used at acoustic emission frequencies lower than 20 kHz.

### *2.d.2) Quiet-scanning System*

The step motors used in the present scanner produce loud audio noise that interferes with the acoustic emission produced by the object. To reduce the vibration and acoustic noise of the scanning, a new scanning system is being designed that is based on analog servo motors instead of the present step motors. The new scanning system has optically encoded axes for precise positioning. This system is currently under construction.

### 2.d.3) Tone Burst Scanning

Tone burst scanning is a method we have used to avoid the ultrasound standing wave effect and acoustic emission multipath effect in the water tank (Table 1).

Ultrasound standing wave effect is caused by multiple reflection of the sound between a highly reflective object and the transducer. Acoustic emission multipath effect is caused by multiple reflection of the acoustic emission by the walls or other reflectors within the tank. Both these phenomena reduce the quality of the final image and can introduce false patterns on the image.

In this method we excite each transducer element with tone bursts of continuous waves. The length of the bursts ( $T_B$ ) is chosen to be at least several times the acoustic emission period,  $2\pi/\Delta\omega$ , but short enough to avoid any overlapping with its multiple reflections from the nearby structures such as the tank walls. Assuming that  $\tau$  represent the time delay between the acoustic emission signal and its reflection coming from the closest structure (which could be the transducer, wall, water surface, etc.), we can write:

$$2\pi/\Delta\omega \ll T_B \ll \tau. \quad (1)$$

There are two major drawbacks for this method. The first problem is limitation on acoustic emission frequency. To satisfy the above equation we often have to use a high acoustic emission frequency, such that:

$$\Delta\omega \gg 2\pi/\tau. \quad (2)$$

In our perimental setup the acoustic emission frequency needs to be about 40 kHz or more.

The second problem is production of unwanted acoustic noise. Applying a sudden burst of energy to a transducer usually produces a transient vibration of the transducer case. This vibration introduces a wideband noise in the entire experimental setup. To reduce this effect, we can use a gradual ascending and descending tone burst, which is described in the next section.

### 2.d.4) Gating Tone Bursts

A "Soft Gate" was constructed using a raised cosine shaping circuit to reduce rise time and fall time of tone burst edges. This approach greatly reduces the acoustic noise from transducer element shock, thus improving the detection threshold of the system.

To test this method, we scanned the RTV glass-bead phantom with and without the soft gate. Without this gate, the noise from the transducer shock overwhelmed the weak acoustic emission from the bead. The image quality was greatly improved and the bead became readily detectable after using the soft gate. Experiments on the RTV phantom with holes also showed the same improvement.

### 2.d.5) Aluminum Free Tank

When imaging small objects such as glass beads (or microcalcifications), the signal level is very low, hence any source of acoustic noise should be studied and hopefully eliminated.

We discovered that pieces made from aluminum can cause a considerable acoustic noise when the piece is placed in water. Clamps, rods, and other structures used for holding the transducer and



the object in the water tank are usually made from aluminum. Chemical interaction of water and aluminum produces a “flickering” sound in the tank. This sound, which is of transient nature but repeated in random pattern, is a wideband noise which can not be filtered out at the frequency range that is of our interest for acoustic emission. Its amplitude is significant compared to the acoustic emission from small objects.

Eliminating all aluminum from the water tank significantly reduced background noise.

## 2.e Modeling and Evaluation of the Acoustic Frequency Responses, $Q(\Delta\omega)$ and $H(\Delta\omega)$

The aim of our method is to image an object based on its mechanical characteristics. This is achieved by vibrating the object by applying a highly localized oscillating force to each point of the object. The localized force is produced by modulating the intensity, and thereby the radiation force, of an ultrasound field at low frequencies (normally in kHz range). The resulting sound emitted by the object is a function of object mechanical characteristics and the location of the excitation point. The image is produced by mapping the amplitude or phase of this sound, which is detected by a sensitive hydrophone, versus position. Figure 1 of reference [1] (page 52) illustrates this method.

In this section we describe the relationship between the image and the properties of the object and the medium. More detail analysis is presented in references [1], [2], and [3].

Here we use the terminology which is used in reference [1] and call this method “Ultrasound-Stimulated Vibro-Acoustography” (USVA). We will also use the notations used in that reference. In particular, we note that  $Q(\Delta\omega)$  is represented by  $Q_{\Delta\omega}$ , and  $H(\Delta\omega)$  is represented by  $H_{\Delta\omega}$ .

Consider a plane ultrasound beam interacting with a planar object of zero thickness and arbitrary shape and boundary impedance that scatters and absorbs. The radiation force vector,  $\mathbf{F}$ , arising from this interaction has a component in the beam direction and another transverse to it. The magnitude of this force is proportional to the average energy density of the incident wave  $\langle E \rangle$  at the object, where  $\langle \rangle$  represents the time average, and  $S$ , the area of the projected portion of the object [6]

$$\mathbf{F} = \mathbf{d}_r S \langle E \rangle, \quad (3)$$

where  $\mathbf{d}_r$  is the vector drag coefficient with a component in the incident beam direction and another transverse to it. The coefficient  $\mathbf{d}_r$  is defined per unit incident energy density and unit projected area. For a planar object,  $\mathbf{d}_r$  is numerically equal to the force on the object. Physically, the drag coefficient represents the scattering and absorbing properties of the object and is given by [6]

$$\mathbf{d}_r = \hat{\mathbf{p}} \frac{1}{S} \left( \Pi_a + \Pi_s - \int \gamma \cos \alpha_s dS \right) + \hat{\mathbf{q}} \frac{1}{S} \int \gamma \sin \alpha_s dS, \quad (4)$$

where  $\hat{\mathbf{p}}$  and  $\hat{\mathbf{q}}$  are the unit vectors in the beam direction and normal to it, respectively. The quantities  $\Pi_a$  and  $\Pi_s$  are the total absorbed and scattered powers, respectively, and  $\gamma$  is the scattered intensity, all expressed per unit incident intensity. Also,  $\alpha_s$  is the angle between the incident and the scattered intensity, and  $dS$  is the area element. The drag coefficient can also be interpreted as the ratio of the radiation force magnitude on a given object to the corresponding value if the object were replaced by a totally absorbing object of similar size. This is because  $|\mathbf{d}_r| = 1$  for a totally absorbing object. This coefficient can be determined for objects of different shapes and sizes. For simplicity, we assume a planar object normal to the beam axis. In this case, the transverse component vanishes,

thus, the drag coefficient (force) will have only a component normal to the target surface which we denote by scalar  $d_r$  ( $F$ ).

To produce a dynamic radiation force, one can use an amplitude modulated beam [7]. Consider an amplitude modulated incident (ultrasonic) pressure field,  $p(t)$ , as

$$p(t) = P_{\omega_0} \cos(\Delta\omega t/2) \cos \omega_0 t, \quad (5)$$

where  $P_{\omega_0}$ ,  $\Delta\omega/2$ , and  $\omega_0$  are the pressure amplitude, modulating frequency, and the center frequency, respectively. In our analysis and experiments, we assume that the condition  $\Delta\omega \ll \omega_0$  holds. In such a case, the energy density of the incident field has slow variations in time. To discriminate the slow time variations of a function, let us define the *short-term time average* of an arbitrary function  $\xi(t)$  over the interval of  $T$  seconds at time instance  $t$ , as  $\langle \xi(t) \rangle_T = \frac{1}{T} \int_{t-T/2}^{t+T/2} \xi(\tau) d\tau$ , which is a function of  $t$ . The long-term time average (or simply, the time average) is obtained by setting  $T \rightarrow \infty$ . To compute the short-term time average of the acoustic energy density relevant to field variations at  $\Delta\omega/2$ , we choose  $T$  longer than the ultrasound wave period but much shorter than the modulation period, that is  $2\pi/\omega_0 \ll T \ll 4\pi/\Delta\omega$ . Under this condition, the short-term time average of  $p^2(t)$  is  $\langle p^2(t) \rangle_T = \frac{P_{\omega_0}^2}{4} (1 + \cos \Delta\omega t)$ . The energy density is given by  $p^2(t)/\rho c^2$  where  $\rho$  and  $c$  are the density and propagation speed in the medium [8]. We are interested in the time-varying component of the short-term time average of the energy density. Denoting this component by  $e_{\Delta\omega}(t)$ , we can write:  $e_{\Delta\omega}(t) = \frac{P_{\omega_0}^2}{4\rho c^2} \cos \Delta\omega t$ . This component of the energy density produces a time varying radiation force on the target (Eq. 3) at frequency  $\Delta\omega$ . The amplitude of this force,  $F_{\Delta\omega}$ , is

$$F_{\Delta\omega} = \frac{P_{\omega_0}^2}{4\rho c^2} S d_r. \quad (6)$$

This equation states that the time-varying force amplitude is proportional to the square of incident ultrasound pressure, or equivalently, to the incident power. If the object moves in response to this force, then the high-frequency ultrasound energy would convert to low-frequency mechanical energy.

The radiation force  $F_{\Delta\omega}$  vibrates the target object at frequency  $\Delta\omega$ . Object vibration results in an acoustic field in the medium (acoustic emission). This field is related to object shape, size, and viscoelastic properties. To present a conclusive analysis of this relationship, we have to assume an object with specific characteristics. Here, we assume that the vibrating object has a circular cross section of radius  $b$  and uniformly vibrates back and forth like a piston. This choice allows us to illustrate the concept in a simple form. We also consider an area  $S \leq \pi b^2$  of the piston surface to be projected normally by the beam. Similar solutions can be carried out for other objects.

The steady state normal velocity amplitude of a piston,  $U_{\Delta\omega}$ , due to a harmonic force  $F_{\Delta\omega}$  at frequency  $\Delta\omega$ , can be described in terms of the mechanical impedance  $Z_{\Delta\omega}$ ,

$$U_{\Delta\omega} = \frac{F_{\Delta\omega}}{Z_{\Delta\omega}}, \quad (7)$$

where  $Z_{\Delta\omega} = Z'_m + Z_r$  is comprised of the mechanical impedance of the object in vacuum  $Z'_m$ , and the radiation impedance of the object  $Z_r$ , all defined at  $\Delta\omega$ . Modeling the object as a mass-spring

system,  $Z'_m$  can be written in terms of  $\Delta\omega$  as

$$Z'_m = R'_m - j \left( m\Delta\omega - \frac{K'}{\Delta\omega} \right), \quad (8)$$

where  $m$ ,  $R'_m$ , and  $K'$  are the mass, mechanical resistance, and the spring constants of the object, respectively. The radiation impedance of the piston can be written as [9]

$$Z_r = \pi b^2 (R_r - jX_r), \quad (9)$$

where

$$R_r = \rho c \left[ 1 - \frac{c}{\Delta\omega b} J_1 \left( \frac{c}{2\Delta\omega b} \right) \right], \quad (10)$$

and

$$X_r = \frac{4\rho c}{\pi} \int_0^{\frac{\pi}{2}} \sin \left( \frac{2\Delta\omega b}{c} \cos \alpha \right) \sin^2 \alpha d\alpha, \quad (11)$$

where  $J_1(\cdot)$  is the first-order Bessel function of the first kind. In many applications of our interest, the wavelength is much greater than the object size, hence,  $\frac{\Delta\omega}{c}b \rightarrow 0$ . In such cases  $Z_r$  assumes a simpler form:

$$Z_r = \pi b^3 \rho \Delta\omega \left( \frac{\Delta\omega b}{2c} - j \frac{8}{3\pi} \right). \quad (12)$$

The mechanical impedance of the piston object can now be written as

$$\begin{aligned} Z_{\Delta\omega} &= (R'_m + \pi b^2 R_r) - j \left( m\Delta\omega - \frac{K'}{\Delta\omega} + \pi b^2 X_r \right) \\ &\approx \left( R'_m + \frac{\pi \rho}{2c} b^4 \Delta\omega^2 \right) - j \left( m\Delta\omega - \frac{K'}{\Delta\omega} + \frac{8}{3} \rho b^3 \Delta\omega \right), \quad \frac{\Delta\omega b}{c} \rightarrow 0. \end{aligned} \quad (13)$$

Once we calculate  $U_{\Delta\omega}$ , we can calculate the pressure field it produces in the medium. We assume that the acoustic emission signal propagates in a free and homogenous medium. The farfield acoustic pressure due to a piston source of radius  $b$  set in a planar boundary of infinite extent is given by [9],

$$P_{\Delta\omega} = -j\Delta\omega\rho \frac{\exp(j\Delta\omega l/c)}{4\pi l} \left[ \frac{2J_1\left(\frac{\Delta\omega b}{c} \sin \vartheta\right)}{\frac{\Delta\omega b}{c} \sin \vartheta} \times \frac{\cos \vartheta}{\cos \vartheta + \beta_B} \right] (2\pi b^2 U_{\Delta\omega}), \quad (14)$$

where  $l$  is the distance from the observation point to the center of the piston,  $\vartheta$  is the angle between this line and the piston axis, and  $\beta_B$  is the specific acoustic admittance of the boundary surface. The specific acoustic admittance is  $\beta_B = \frac{\rho c}{Z_B}$ , where  $Z_B$ , the acoustic impedance of the boundary, represents the ratio between the pressure and normal fluid velocity at a point on the surface. The factor of two comes from the presence of the boundary wall. It would be replaced by unity if the boundary wall were not present [8]. The acoustic emission field resulting from object vibration can be written in terms of the incident ultrasound pressure by combining Eqs. 6, 7, and 14, as

$$\begin{aligned} P_{\Delta\omega} &= \left\{ j \frac{\Delta\omega}{c^2} \times \frac{\exp(j\Delta\omega l/c)}{4\pi l} \left[ \frac{2J_1\left(\frac{\Delta\omega b}{c} \sin \vartheta\right)}{\frac{\Delta\omega b}{c} \sin \vartheta} \times \frac{\cos \vartheta}{\cos \vartheta + \beta_B} \right] \right\} \\ &\times \left[ \frac{1}{(R'_m + \pi b^2 R_r) - j \left( m\Delta\omega - \frac{K'}{\Delta\omega} + \pi b^2 X_r \right)} \right] (2\pi b^2) P_{\omega_0}^2 S d_r, \end{aligned} \quad (15)$$



For wavelengths that are long compared to the object size, i.e., when  $b\Delta\omega/c \rightarrow 0$ , the term in the first brace approaches a constant, hence we may consider the contents of the first brace to be an object independent function (the specific acoustic admittance  $\beta_B$  relates to the surrounding boundary surface). Under these conditions, the first brace in the above equation represents the effect of the medium on the acoustic emission field, which we may call the *medium transfer function*, and denote it by

$$H_{\Delta\omega}(l) = j \frac{\Delta\omega}{c^2} \times \frac{\exp(j\Delta\omega l/c)}{4\pi l} \left[ \frac{2J_1\left(\frac{\Delta\omega b}{c} \sin \vartheta\right)}{\frac{\Delta\omega b}{c} \sin \vartheta} \times \frac{\cos \vartheta}{\cos \vartheta + \beta_B} \right]. \quad (16)$$

The second bracket in Eq. 15 is  $\frac{1}{Z_{\Delta\omega}}$ , or the mechanical admittance of the object at the frequency of the acoustic emission ( $\Delta\omega$ ), and we denote it by  $Y_{\Delta\omega}$ . It is convenient to combine this term with the next term ( $2\pi b^2$ ) in Eq. 15, as  $Q_{\Delta\omega} = 2\pi b^2 Y_{\Delta\omega} = 2\pi b^2 / Z_{\Delta\omega}$ , which is the total acoustic outflow<sup>1</sup> by the object per unit force. Function  $Q_{\Delta\omega}$  represents the object characteristics at the acoustic frequency. We may thus rewrite Eq. 15 in a more compact form as

$$P_{\Delta\omega} = H_{\Delta\omega}(l) Q_{\Delta\omega} P_{\omega_0}^2 S d_r. \quad (17)$$

Equation 17 indicates that the acoustic emission pressure is proportional to: 1) the square of ultrasound pressure  $P_{\omega_0}$ , 2) the ultrasound characteristics of the object,  $d_r$ , in the projected area  $S$ , 3) the acoustic outflow by this object,  $Q_{\Delta\omega}$ , representing the object size  $b$  and its mechanical admittance at the acoustic frequency,  $Y_{\Delta\omega}$ , and 4) the transfer function of the medium at the acoustic frequency,  $H_{\Delta\omega}(l)$ . The above equation illustrates the basic nonlinear relationship between the ultrasound and acoustic emission pressure amplitudes. Note that neither the medium nor the object need to be nonlinear for this relationship to hold. It is interesting to note that the projection area  $S$  and the vibrating area  $\pi b^2$  play different roles. The projection area determines the extent of the force applied to the object (Eq. 6). The vibrating area, however, influences the total acoustic outflow in the medium caused by object vibration. The mechanism of object vibration is somewhat analogous to that of a loudspeaker, where the electromotive force is exerted to a small area of the membrane (usually at the center) causing the entire membrane surface to vibrate. In our method, the size of the vibrating area depends on the object structure. For a free suspended point object, smaller than the beam cross section, the vibrating area would be the same as the projection area. For a large stiff plate, however, the vibrating area could be much larger than the projected area (similar to a loudspeaker). In some cases it is more convenient to have the acoustic emission field in terms of the applied force  $F_{\Delta\omega}$ . Referring to Eq. 6, we can rewrite Eq. 17 as

$$P_{\Delta\omega} = 4\rho c^2 H_{\Delta\omega}(l) Q_{\Delta\omega} F_{\Delta\omega}. \quad (18)$$

Again in analogy to a loudspeaker,  $F_{\Delta\omega}$ ,  $Q_{\Delta\omega}$ , and  $H_{\Delta\omega}(l)$  represent the electromotive force, dynamic characteristics of the membrane, and the propagation medium transfer function.

<sup>1</sup> Acoustic outflow is the volume of the medium (e.g., the fluid) in front of the object surface that is displaced per unit time due to object vibration.

## 2.f Beam Forming: Modeling and Experimental Results

Beam forming for our method is basically different from that used in the conventional ultrasound system. In a conventional pulse-echo system beam forming is done to produce the smallest possible beam width with the highest intensity. Here we are interested in producing a radiation stress field in a small region in a three-dimensional space.

We have developed three beam forming methods: (1) single modulated beam, (2) two crossing beam (x-focal), and (3) the confocal beams. The single beam is of theoretical interest and is not used in our practice because of its low depth selectivity. The theory of confocal beam is explained in reference [1]. The theory and experimental results for the x-focal beam and a comparison with the other two beams is presented in [4]. Here we mainly present the theory of the confocal beam, which is of the most interest in our experimental work.

Confocal beam is produced by projecting two coaxial, confocal, continuous wave (CW) ultrasound beams on the object. An amplitude modulated field is produced only at the interference region of the two unmodulated beams around their focal areas, resulting in a small resolution cell. For this purpose, elements of a two-element spherically focused annular array (consisting of a central disc with radius  $a_1$  and an outer ring with the inner radius of  $a'_2$  and outer radius of  $a_2$ ) are excited by separate CW signals at frequencies  $\omega_1 = \omega_0 - \Delta\omega/2$  and  $\omega_2 = \omega_0 + \Delta\omega/2$ . We assume that the beams are propagating in a lossless medium, in the  $+z$  direction of a Cartesian coordinate system  $(x, y, z)$ , with the joint focal point at  $z = 0$ . The resultant pressure field on the  $z = 0$  plane may be written as

$$p(t) = P_1(r) \cos(\omega_1 t + \psi_1(r)) + P_2(r) \cos(\omega_2 t + \psi_2(r)), \quad (19)$$

where  $r = \sqrt{x^2 + y^2}$  is the radial distance. The amplitude functions are [8, 10]

$$P_1(r) = \rho c U_{01} \frac{\pi a_1^2}{\lambda_1 z_0} \text{jinc}\left(\frac{r a_1}{\lambda_1 z_0}\right), \quad (20)$$

and

$$P_2(r) = \rho c U_{02} \frac{\pi}{\lambda_2 z_0} \left[ a_2^2 \text{jinc}\left(\frac{r a_2}{\lambda_2 z_0}\right) - a_2'^2 \text{jinc}\left(\frac{r a_2'}{\lambda_2 z_0}\right) \right], \quad (21)$$

where  $\lambda_i = 2\pi/\omega_i$ ,  $i=1, 2$ , is the ultrasound wavelength,  $U_{0i}$  is the particle velocity amplitude at the  $i$ -th transducer element surface, and  $\text{jinc}(X) = J_1(2\pi X)/\pi X$ . The phase functions,  $\psi_i(r) = -\frac{\pi r^2}{\lambda_i z_0}$ , for  $i=1, 2$ , are conveniently set to be zero at the origin.

Now, we define a *unit point target* at position  $(x_0, y_0)$  on the focal plane with a drag coefficient distribution as

$$d_r(x, y) = \delta(x - x_0, y - y_0), \quad (22)$$

such that  $d_r(x, y) dx dy$  is unity at the  $(x_0, y_0)$  and zero elsewhere. This equation is merely used as a mathematical model because  $d_r$  is physically finite. In this case, the projected area can be considered to be  $S = dx dy$ . We replace  $d_r S$  in Eq. 3 with  $d_r(x, y) dx dy$ , and follow the steps similar to those outlined in Eqs. 5 and 6 for the pressure field expressed by Eq. 19, then the complex amplitude of the normal component of the force on the unit point target can be found as

$$F_{\Delta\omega}(x_0, y_0) = \frac{1}{4} \rho U_{01} U_{02} \frac{\pi a_1^2}{\lambda_1 z_0} \text{jinc}\left(\frac{r_0 a_1}{\lambda_1 z_0}\right) \left[ \frac{\pi a_2^2}{\lambda_2 z_0} \text{jinc}\left(\frac{r_0 a_2}{\lambda_2 z_0}\right) - \frac{\pi a_2'^2}{\lambda_2 z_0} \text{jinc}\left(\frac{r_0 a_2'}{\lambda_2 z_0}\right) \right] \times \exp\left(-j \frac{r_0^2 \Delta\omega}{2c z_0}\right), \quad (23)$$

where the arguments  $x_0$  and  $y_0$  are added to denote the position of the point target, and  $r_0 = \sqrt{x_0^2 + y_0^2}$ . Equation 23 describes the spatial distribution of the force (the stress field). This equation shows that the stress field is confined to the regions near the beam axis ( $r_0 = 0$ ), and decays as the radial distance  $r_0$  increases. The lateral extent of the stress field, and hence the resolution cell diameter, would be smaller at higher ultrasound frequencies (smaller  $\lambda_1$  and  $\lambda_2$ ). One can calculate the total force on an arbitrary object by integrating the force over the projected area. The axial extent of the resolution cell (depth resolution, or the depth of field) can be determined by calculating the force  $F_{\Delta\omega}$  as a function of the depth variable, in a fashion as outlined in Eqs. 19 to 23.

## 2.g Point Spread Function

To produce an image we scan the object in a plane and record the complex amplitude of the acoustic emission,  $P_{\Delta\omega}$ , at different positions. In this process, we keep  $\Delta\omega$  fixed. For transverse view images, the scan plane is the focal plane ( $x - y$ ). Alternatively, for the parallel view the scan plane is the  $x - z$  plane. In the conventional ultrasound imaging context, these two views are called the C-scan and B-scan, respectively. Our main focus here is the transverse view imaging. In this case, the acoustic emission data obtained by vibrating the object at point  $(x, y)$  are assigned to the corresponding point  $(x, y)$  in the image.

Before defining the image, we need to define the function that represents the object. Referring to Eq. 17, the terms that are object dependent are the drag coefficient  $d_r$  and the function  $Q_{\Delta\omega}$  (assuming that  $H_{\Delta\omega}(l)$  is object independent). The object function  $g(x, y)$  is thus defined as the spatial distribution of these terms,

$$g(x, y) = Q_{\Delta\omega}(x, y)d_r(x, y). \quad (24)$$

Variables  $x$  and  $y$  are added to denote the dependency of  $d_r$  and  $Q_{\Delta\omega}$  on position. In particular,  $Q_{\Delta\omega}(x, y)$  implies the total acoustic outflow by the object when the force is applied at point  $(x, y)$ .

Commonly, an imaging system is studied through its point spread function (PSF), which is defined as the image of a point object. To determine the PSF of our system, we consider a unit point target at the origin with unit mechanical response,  $Q_{\Delta\omega}(x, y) = 1$ . Hence, referring to Eqs. 22 and 24, we can write  $g(x, y) = \delta(x, y)$ . To obtain the PSF, we move this point object to every possible position  $(x_0, y_0)$  on the  $z = 0$  plane and form the image using the resulting acoustic emission field,  $P_{\Delta\omega}(x_0, y_0)$ . Since  $x_0$  and  $y_0$  are now being treated as variables, we may replace them by variables  $x$  and  $y$ , respectively. We define the normalized PSF of the coherent imaging system as the complex function

$$h(x, y) = P_{\Delta\omega}(x, y)/P_{\Delta\omega}(0, 0). \quad (25)$$

Division by  $P_{\Delta\omega}(0, 0)$  cancels the constant multipliers. Referring to Eqs. 18 and 23, we can write

$$h(x, y) = \frac{1}{a_2^2 - a_2'^2} \text{jinc}\left(\frac{ra_1}{\lambda_1 z_0}\right) \left[ a_2^2 \text{jinc}\left(\frac{ra_2}{\lambda_2 z_0}\right) - a_2'^2 \text{jinc}\left(\frac{ra_2'}{\lambda_2 z_0}\right) \right] \exp\left(-j\frac{r^2 \Delta\omega}{2cz_0}\right). \quad (26)$$

This equation illustrates that the system PSF is a circularly symmetric function with the peak at the origin and decaying amplitude with increasing radial distance  $r$ . Amplitude decays faster for higher ultrasound frequency. This function will be discussed further in the next section.

where the arguments  $x_0$  and  $y_0$  are added to denote the position of the point target, and  $r_0 = \sqrt{x_0^2 + y_0^2}$ . Equation 23 describes the spatial distribution of the force (the stress field). This equation shows that the stress field is confined to the regions near the beam axis ( $r_0 = 0$ ), and decays as the radial distance  $r_0$  increases. The lateral extent of the stress field, and hence the resolution cell diameter, would be smaller at higher ultrasound frequencies (smaller  $\lambda_1$  and  $\lambda_2$ ). One can calculate the total force on an arbitrary object by integrating the force over the projected area. The axial extent of the resolution cell (depth resolution, or the depth of field) can be determined by calculating the force  $F_{\Delta\omega}$  as a function of the depth variable, in a fashion as outlined in Eqs. 19 to 23.

## 2.g Point Spread Function

To produce an image we scan the object in a plane and record the complex amplitude of the acoustic emission,  $P_{\Delta\omega}$ , at different positions. In this process, we keep  $\Delta\omega$  fixed. For transverse view images, the scan plane is the focal plane ( $x - y$ ). Alternatively, for the parallel view the scan plane is the  $x - z$  plane. In the conventional ultrasound imaging context, these two views are called the C-scan and B-scan, respectively. Our main focus here is the transverse view imaging. In this case, the acoustic emission data obtained by vibrating the object at point  $(x, y)$  are assigned to the corresponding point  $(x, y)$  in the image.

Before defining the image, we need to define the function that represents the object. Referring to Eq. 17, the terms that are object dependent are the drag coefficient  $d_r$  and the function  $Q_{\Delta\omega}$  (assuming that  $H_{\Delta\omega}(l)$  is object independent). The object function  $g(x, y)$  is thus defined as the spatial distribution of these terms,

$$g(x, y) = Q_{\Delta\omega}(x, y)d_r(x, y). \quad (24)$$

Variables  $x$  and  $y$  are added to denote the dependency of  $d_r$  and  $Q_{\Delta\omega}$  on position. In particular,  $Q_{\Delta\omega}(x, y)$  implies the total acoustic outflow by the object when the force is applied at point  $(x, y)$ .

Commonly, an imaging system is studied through its point spread function (PSF), which is defined as the image of a point object. To determine the PSF of our system, we consider a unit point target at the origin with unit mechanical response,  $Q_{\Delta\omega}(x, y) = 1$ . Hence, referring to Eqs. 22 and 24, we can write  $g(x, y) = \delta(x, y)$ . To obtain the PSF, we move this point object to every possible position  $(x_0, y_0)$  on the  $z = 0$  plane and form the image using the resulting acoustic emission field,  $P_{\Delta\omega}(x_0, y_0)$ . Since  $x_0$  and  $y_0$  are now being treated as variables, we may replace them by variables  $x$  and  $y$ , respectively. We define the normalized PSF of the coherent imaging system as the complex function

$$h(x, y) = P_{\Delta\omega}(x, y)/P_{\Delta\omega}(0, 0). \quad (25)$$

Division by  $P_{\Delta\omega}(0, 0)$  cancels the constant multipliers. Referring to Eqs. 18 and 23, we can write

$$h(x, y) = \frac{1}{a_2^2 - a_2'^2} \text{jinc}\left(\frac{ra_1}{\lambda_1 z_0}\right) \left[ a_2^2 \text{jinc}\left(\frac{ra_2}{\lambda_2 z_0}\right) - a_2'^2 \text{jinc}\left(\frac{ra_2'}{\lambda_2 z_0}\right) \right] \exp\left(-j\frac{r^2 \Delta\omega}{2cz_0}\right). \quad (26)$$

This equation illustrates that the system PSF is a circularly symmetric function with the peak at the origin and decaying amplitude with increasing radial distance  $r$ . Amplitude decays faster for higher ultrasound frequency. This function will be discussed further in the next section.

## **2.j Discussion**

The theory presented here clarifies the fundamental relationships between the object parameters and its USAE image. This theory indicates that the acoustic emission from an object is related to its mechanical admittance and the size of the object (which acts as a source of acoustic emission). Noting that microcalcifications are very small in size, detecting the acoustic emission field from such a small source becomes a challenge. Hence, to improve the detectability, the acoustic noise in the medium must be minimized. This includes the ambient noise, noise from the scanner, vibrations produced by the transducer body, etc. The improvements that we have made in the laboratory setup, including using the quiet room, air table, absorbing material, soft gate, etc., have enabled us to considerably increase the signal-to-noise ratio of our data. Now, with our low noise setup, we can detect glass beads in RTV material. This was not possible before making these improvements. These results are in support of the initial hypothesis that USAE can be used to detect particles of small size in a viscoelastic material. Using the tone burst method has enabled us to eliminate the standing wave problem at the expense of working at a higher acoustic emission frequency. We need to investigate other methods, such as using a flat annular array transducer, to be able to reduce ultrasound standing waves when working at lower acoustic emission frequencies. Driving a particle at its resonance could enhance detectability and selectivity. That is because at resonance, particle motion is at its maximum. Also, because the resonance frequency of a particle depends on its size and mass, this method can be used to selectively detect particles of particular size and mass. Particle resonance is another subject of interest that remains to be studied further.

## **2.k Key Research Accomplishments**

- Development of the theoretical model describing the relation between the acoustic emission field and the mechanical parameters of the object, as well as to the parameters of the propagation media.
- Developing the theory describing the point spread function of the imaging system with three different beamforming methods.
- Improvement of the sensitivity of the system to detect small particles in a viscoelastic medium. Now we can detect a glass bead with diameter of  $260\ \mu\text{m}$  (mimicking a microcalcification) in gel (mimicking soft tissue).
- Identifying causes of image artifacts, such as ultrasound standing wave, multipath, and reverberation of acoustic emission.
- Developing methods for reducing or eliminating acoustic emission multipath and reverberation problems.
- Developing methods for reducing acoustic and vibrational noise in the system

## **2.l Reportable Outcomes**

1. Fatemi, M., and J. F. Greenleaf: Ultrasound-stimulated vibro-acoustic spectrography. *Science* 280:82–85, April 3, 1998 (pages 24–27 of this report).
2. Fatemi, M., and J. F. Greenleaf: Vibro-acoustography: An imaging modality based on ultrasound-stimulated acoustic emission. *proceedings of the National Academy of Sciences USA* (In Press) (pages 28–56 of this report).

3. Fatemi, M., and J. F. Greenleaf: Potential applications of ultrasound-stimulated vibro-acoustography in medical diagnosis and material characterization. 137th Meeting of the Acoustical Society of America and 2nd Convention of the European Acoustical Association, Berlin, Germany, March 14–19, 1999 (Invited presentation) (page 58 of this report).
4. Fatemi, M., and J. F. Greenleaf: Beam forming for ultrasound-stimulated vibro-acoustography. ICTCA'99 Fourth International Conference on Theoretical and Computational Acoustics, Trieste, Italy, May 10–14, 1999 (Keynote presentation) (page 59 of this report).

## 2.m Conclusions

In this report we presented analytical relationships that relate the acoustic emission field to the mechanical parameters of object. This model provides a tool for better understanding of the USAE imaging, as well as for characterizing objects in terms of their mechanical parameters. Noting that the mechanical stiffness of breast microcalcification is drastically different from that of soft tissue, characterizing microcalcifications based on their mechanical parameters is of particular interest. We have also presented the point spread function of the imaging system by which we can model the system. We have shown that the experimental system can be improved to be able to image small particles, about the size of breast microcalcifications, in a viscoelastic medium.

### 2.m.1) *So what?*

We have shown that ultrasound-stimulated acoustic emission method (or vibro-acoustography) is capable of detecting small particles in a viscoelastic medium. Improvement of this technique such that it can be used to reliably detect breast microcalcifications would be a significant contribution for breast cancer detection. This tool may particularly be of interest in examining dense breasts, or pregnant patients, where x-ray mammography cannot be used.

## 2.n References

1. Fatemi, M., and J. F. Greenleaf: Vibro-acoustography: An imaging modality based on ultrasound-stimulated acoustic emission. Proceedings of the National Academy of Sciences USA (In Press).
2. Fatemi, M., and J. F. Greenleaf: Ultrasound-stimulated vibro-acoustic spectrography. *Science* 280:82–85, April 3, 1999.
3. Fatemi, M., and J. F. Greenleaf: Potential applications of ultrasound-stimulated vibro-acoustography in medical diagnosis and material characterization. 137th Meeting of the Acoustical Society of America and 2nd Convention of the European Acoustical Association, Berlin, Germany, March 14–18, 1999 (Invited Abstract).
4. Fatemi, M., and J. F. Greenleaf: Beam forming for ultrasound-stimulated vibro-acoustography. ICTCA'99 Fourth International Conference on Theoretical and Computational Acoustics, Trieste, Italy, May 10–14, 1999 (Keynote Abstract).
5. Fatemi, M., and J. F. Greenleaf: Acoustic field calculation in ultrasound-stimulated vibro-acoustography. Second International Conference on Ultrasound in Medicine and Engineering, Beijing, China, August 26–28, 1998 (Abstract).
6. Westervelt, P. J.: *J Acoust Soc Am* 23(4):312–315, May, 1951.



7. Greenspan, M., F. R. Breckenridge, C. E. Tschiegg: Ultrasonic transducer power output by modulate radiation pressure. *J Acoust Soc Am* 63(4):1031–1038, April, 1978.
8. Morse, P. M., and K. U. Ingard: *Theoretical Acoustics*. McGraw Hill, New York. 1968.
9. Morse, P. M.: *Vibration and Sound*, 3rd edition, The Acoustical Society of America, 1981.
10. Kino, G. S.: *Acoustics Waves: Devices, Imaging, and Analog Signal Processing*, Prentice-Hall Signal Processing Series, Englewood Cliffs, NJ, 1987.

### 3 APPENDICES

**Appendix A:** Figures (pages 21–23 of this report)

**Appendix B:** Fatemi, M., and J. F. Greenleaf: Ultrasound-stimulated vibro-acoustic spectrography. *Science* 280:82–85, April 3, 1998 (pages 24–27 of this report).

**Appendix C:** Fatemi, M., and J. F. Greenleaf: Vibro-acoustography: An imaging modality based on ultrasound-stimulated acoustic emission. proceedings of the National Academy of Sciences USA (In Press) (pages 28–56 of this report).

**Appendix D:** Fatemi, M., and J. F. Greenleaf: Acoustic field calculation in ultrasound-stimulated vibro-acoustography. Second International Conference on Ultrasound in Medicine and Engineering, Beijing, China, August 26–28, 1998 (Abstract) (page 57 of this report)

**Appendix E:** Fatemi, M., and J. F. Greenleaf: Potential applications of ultrasound-stimulated vibro-acoustography in medical diagnosis and material characterization. 137th Meeting of the Acoustical Society of America and 2nd Convention of the European Acoustical Association, Berlin, Germany, March 14–19, 1999 (Invited presentation) (page 58 of this report).

**Appendix F:** Fatemi, M., and J. F. Greenleaf: Beam forming for ultrasound-stimulated vibro-acoustography. ICTCA'99 Fourth International Conference on Theoretical and Computational Acoustics, Trieste, Italy, May 10–14, 1999 (Keynote presentation) (page 59 of this report).

## Figures and Legends

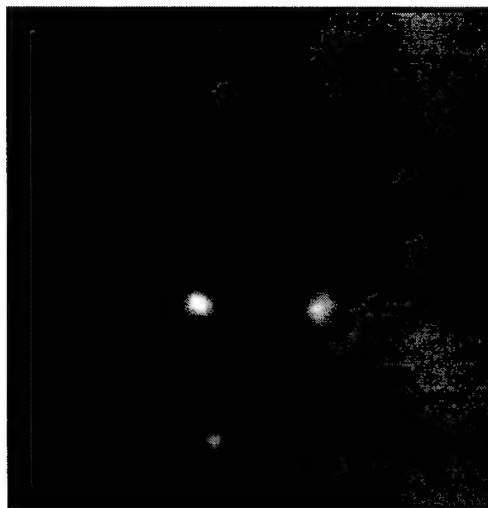


Figure 1 Image of glass beads in gel. This image is obtained by scanning the gel phantom. This image covers an area of 20 mm by 20 mm, scanned at 0.2 mm/pixel. The beads are located about 10 mm deep inside the gel. The diameter of the top bead is about 260  $\mu\text{m}$ , and the diameter of the largest bead is about 400  $\mu\text{m}$ . The image is obtained by tone burst method and using the soft gate. The acoustic emission frequency was set at 53.5 KHz.



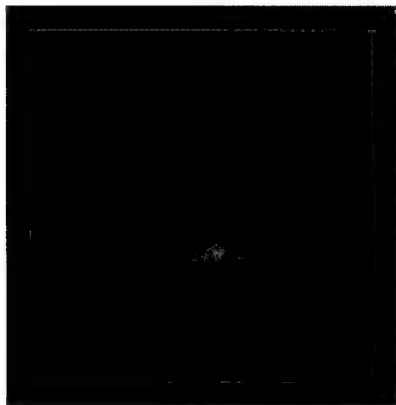


Figure 2 Image of a glass bead in RTV. This image is obtained by scanning the RTV phantom containing glass bead. The image covers an area of 10x10 mm and is scanned at 0.1 mm increments. The glass bead is located at 3 mm from the surface of the phantom, and its diameter is about 350  $\mu\text{m}$ . The image is obtained by tone burst method and using the soft gate. The acoustic emission frequency was set at 46.6 KHz.

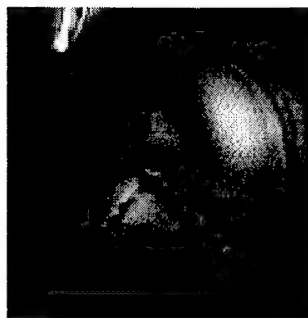


Figure 3 Image of holes in RTV. This image covers a square of 60x60 mm, and is scanned at 0.3 mm/pixel. The two holes (diameters about 2 mm) are located at 3 mm and 10 mm from the surface. The ultrasound beam was focused near the surface of the phantom. The image is obtained by tone burst method and using the soft gate. The acoustic emission frequency was set at 50 KHz.

# Ultrasound-Stimulated Vibro-Acoustic Spectrography

Mostafa Fatemi and James F. Greenleaf

An ultrasound method based on radiation force is presented for imaging the acoustic response of a material to mechanical excitation. Acoustic energy was emitted from solids and tissues in response to an oscillatory radiation force produced by interfering focused beams of ultrasound. Frequency spectra of ultrasound-stimulated acoustic emission exhibited object resonances. Raster-scanning the radiation force over the object and recording the amplitude and phase of the emitted sound resulted in data from which images related to the elastic compositions of the acoustically emitting objects could be computed. Acoustic emission signals distinguished tuning-fork resonances, submillimeter glass spheres, and calcification in excised arteries and detected object motions on the order of nanometers.

The mechanical response of objects to external forces is of considerable interest in medical diagnosis, nondestructive inspection of materials, and materials science. An applied force is often used to produce displacement from which elastic constants, like spring constants, can be determined. In resonant ultrasound spectroscopy, an ultrasound source and a detector are used to measure the resonance frequencies of a sample with known size and mass. The resonances are related to mechanical parameters, including the elastic constants of the material (1). Recently, a magnetic resonance elastography method for quantitatively measuring the displacement of tissues in response to externally applied cyclic forces was reported by Muthupillai *et al.* (2). The method resulted in high-resolution images of the shear modulus of normal and pathologic tissues. Others have used ultrasound to measure tissue displacement associated with externally applied compressive and cyclic forces (3).

We describe an imaging technique that uses acoustic emission to map the mechanical response of an object to local cyclic radiation forces produced by interfering ultrasound beams. Radiation force is generated by changes in the energy density of an acoustic field (4). For instance, a collimated ultrasound beam impinging normally on the surface of an object of arbitrary shape and boundary impedance will produce a radiation force. The radiation force arising from this interaction has a component  $F = d_r \langle E \rangle$  (5) in the beam direction. This component is proportional to the time-average energy density of the incident wave  $\langle E \rangle$ , the projected area of the object  $s$ , and  $d_r$  (6), the scattering and absorbing properties of the object.

We probe the object by arranging the intersection of two focused continuous-

wave (CW) ultrasound beams of different frequencies at a selected point on the object. Interference in the intersection region of the two beams produces sinusoidal modulation of the ultrasound energy density. Modulation of the energy density creates an oscillatory force, effectively vibrating the object at the selected region. The resulting vibration of the object produces an acoustic field [acoustic emission (7)] that can be measured some distance away.

Ultrasound beams can be constructed in a variety of ways for this purpose (8). We used two coaxial, confocal transducer elements of a spherically focused annular array (consisting of a central disc and an outer annulus) driven by two CW signals at slightly different frequencies  $\omega_1$  and  $\omega_2$  (Fig. 1). The energy density at a point in this ultrasound field, say at the focus, is proportional to the square of the sum of the ultrasound fields from the two elements. Squaring the sum of two sines gives rise to sum and difference frequency terms. Thus,

high-frequency and low-frequency variations in energy density result at the intersection of the two beams produced by the two elements. Ultrasound-stimulated acoustic emission results from the energy term that produces a low-frequency vibration. The low-frequency force on a target at the focal point can be computed by

$$F_1(t) = d_r \iint_S \langle E_{\text{focal}}(t, x, y) \rangle_T dx dy$$

$$= C d_r \cos(\Delta\omega t) \quad (1)$$

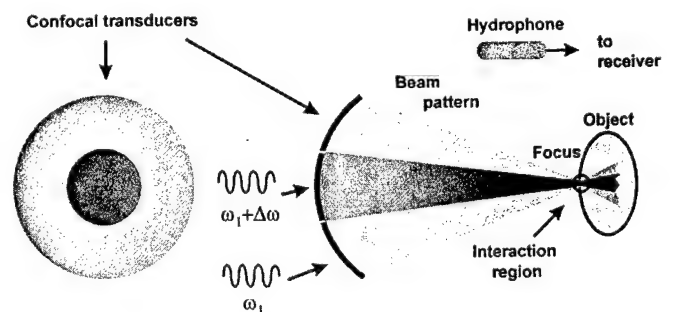
where  $C$  is a constant,  $\Delta\omega = |\omega_1 - \omega_2|$ ,  $S$  is the area over which  $E_{\text{focal}}(t, x, y)$ , the total energy density in the focal plane, has significant value, and  $\langle \rangle_T$  represents a short-term time average (9). For focused beams, the intersection region can be small enough that  $F_1(t)$  can be considered to be an oscillating point force applied to the object at the focal intersection of the beams.

To produce an ultrasound-stimulated vibro-acoustic spectrogram, we vibrate a small region of the object with an oscillating radiation force of varying frequency. The complex amplitude of the resulting acoustic emission field is

$$\Phi(\Delta\omega) = C d_r H(\Delta\omega) Q(\Delta\omega) \quad (2)$$

where  $Q(\Delta\omega)$  is a complex function representing the mechanical frequency response, or admittance, of the object at the selected point, and  $H(\Delta\omega)$  represents the combined frequency response, or transfer function, of the propagation medium and receiver and is assumed to be fixed and known (10). Recording  $\Phi(\Delta\omega)$  allows us to obtain  $Q(\Delta\omega)$  for each point within a constant multiplier (11). We raster-scan the radiation force over the object to produce data, which can

**Fig. 1.** Experimental system for ultrasound-stimulated vibro-acoustic spectrography: a two-element confocal ultrasound annular array transducer, consisting of a center disc and an outer ring. The elements are driven by two CW sources, at frequencies equal to  $\omega_1$  and  $\omega_2 = \omega_1 + \Delta\omega$ , where these frequencies



are very close to the central frequency of the elements, and  $\Delta\omega$  is much smaller than ( $<1\%$ ) the center frequency of the ultrasound transducer. The beams interact only in a small region around the joint focal point, where the amplitude of the field oscillates at the difference frequency  $\Delta\omega$ . The region of interest is placed at the joint focal point and is probed point-by-point by raster scanning. The sound field resulting from object vibrations at each position is received by a hydrophone and recorded. The recorded signal at one or more difference frequencies is used to form an image of the object. The experiments were conducted in a water tank. The transducer center frequency was 3 MHz; its outer diameter was 45 mm; and it was focused at 70 mm. The difference frequencies used in each experiment are mentioned in the corresponding legends.

Ultrasound Research, Department of Physiology and Biophysics, Mayo Clinic and Mayo Foundation, Rochester, MN 55905, USA.

be mapped into a pictorial format. The spatial resolution of the resulting image is determined by the region in which significant interference between the ultrasound beams occurs and is of the order of a few wavelengths at the ultrasound frequency.

Experiments were conducted in a water tank, which provided good ultrasonic and acoustic coupling to the object and freedom of movement for the prototype scanner mechanism (Fig. 1). The two-element confocal ultrasound transducer array was positioned such that the beams interfered at the selected region of the object. Sound produced by vibrations of the object is approximately omnidirectional because of the small size of the vibrating portion of the object compared with the wavelength. This sound was detected by a submerged hydrophone placed near the object within the water tank.

To test the hypothesis that ultrasound-stimulated acoustic emission is sensitive to object mechanical properties and to show how such properties can be quantitatively evaluated by this method, we produced an ultrasound-stimulated vibro-acoustic spectrogram of a tuning fork immersed in isopropyl alcohol at two different temperatures. We aimed the focal point of the confocal transducer at a fixed position on one of the tines. The shear viscosity of alcohol changes with temperature, causing a slight, but detectable, shift in the spectrogram (Fig. 2). The shear viscosity  $\eta$  of a liquid is determined by measuring the resonant frequency  $f_R$  and the bandwidth  $\delta f_R$  of a tuning fork immersed in this liquid (12)

$$\eta = \frac{\kappa f_R}{\rho} \left( \frac{\delta f_R}{f_R} - \frac{\delta f_{R0}}{f_{R0}} \right)^2 \quad (3)$$

where  $f_{R0}$  and  $\delta f_{R0}$  are the resonant fre-

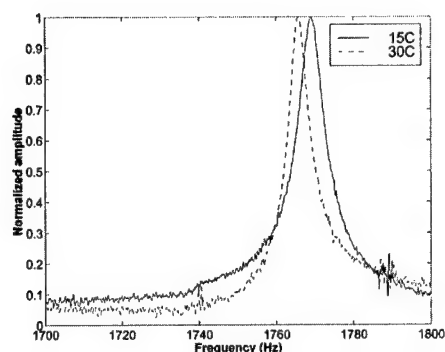


**Fig. 2.** Vibro-acoustic spectrograms of a tuning fork immersed in isopropyl alcohol at two different temperatures. A point on a tine of the fork was vibrated with the use of the system shown in Fig. 1. The difference frequency was swept from 1600 to 2000 Hz. A change of temperature from 15° to 30°C decreases the shear viscosity of the alcohol, which, in turn, changes the resonance frequency and bandwidth of the tuning fork.

quency and bandwidth measured in vacuum, respectively, and  $\rho$  is the liquid density. The constant  $\kappa$  is determined experimentally. The measured values for  $f_R$  and  $\delta f_R$  were 1769 and 5.76 Hz at 15°C and 1765.7 and 4.53 Hz at 30°C. The viscosity of isopropyl alcohol is reported to be 2.89 cP (1 centipoise = 1 mPa·s) at 15°C (13). From this value, the constant  $\kappa$  was calculated. The shear viscosity at 30°C was found using Eq. 3 to be  $\eta = 1.77$  cP, which is the same as the published data (13).

We tested the ability of ultrasonically stimulated vibro-acoustic spectrography to image the frequency response of different objects with identical  $d_t$  by scanning three tuning forks with different resonant frequencies. A color acoustic spectrogram was obtained by sweeping the frequency of the radiation force,  $\Delta\omega$ , in a range covering the resonant frequencies of all forks at each beam position. The acoustic emission signal was filtered by three bandpass filters centered at different frequencies. The outputs of these filters were used to form a three-color composite image (Fig. 3). The forks appear

with three distinct colors because each fork responds primarily at its own resonant frequency. Because the forks were made from identical materials, other ultrasound imaging methods would not be capable of distinguishing these objects.

We tested the hypothesis that the amplitude of acoustic emission at a single frequency can be used to detect small, highly reflective isolated objects. We scanned a 380- $\mu$ m-diameter glass bead placed on a thin latex sheet and recorded the amplitude of acoustic emission (Fig. 4). The latex sheet produces only a small change in the incident energy because it is almost transparent to the ultrasound beam. This experiment demonstrated the ability of the method to detect isolated regions of hardness with respect to a soft background.

To test the feasibility of using the technique to image mechanical properties of tissues, we measured the phase and amplitude of acoustic emission from calcified and noncalcified excised human iliac arteries. The arteries were scanned in a plane perpendicular to the ultrasound beam axis.

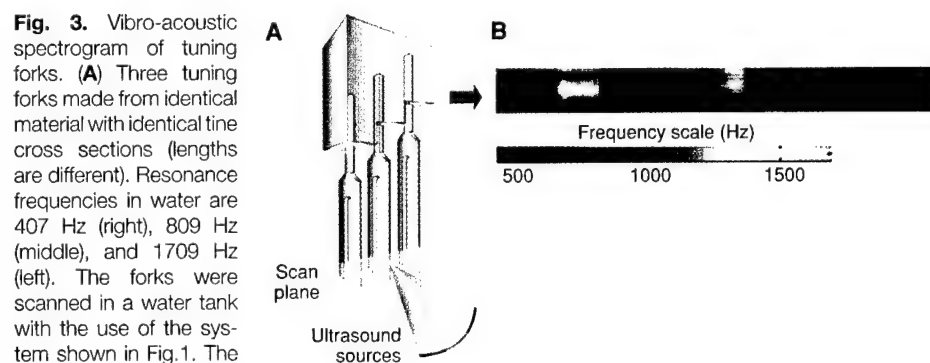


**Fig. 3.** Vibro-acoustic spectrogram of tuning forks. (A) Three tuning forks made from identical material with identical tine cross sections (lengths are different). Resonance frequencies in water are 407 Hz (right), 809 Hz (middle), and 1709 Hz (left). The forks were scanned in a water tank with the use of the system shown in Fig. 1. The scanning plane covers the front tines at the bottom part of the forks. At each position, the difference frequency was swept from 250 to 2250 Hz. The ultrasound-stimulated acoustic emission was detected with the hydrophone and filtered by three overlapping bandpass filters with frequencies centered at 500, 1000, and 1500 kHz, respectively. (B) Color acoustic spectrogram of the forks. The outputs of the bandpass filters were used to produce the red, green, and blue image components. This image displays two characteristics of the object: shape and frequency response. The color associated with each fork indicates its resonance frequency, which can be deduced from the frequency scale.

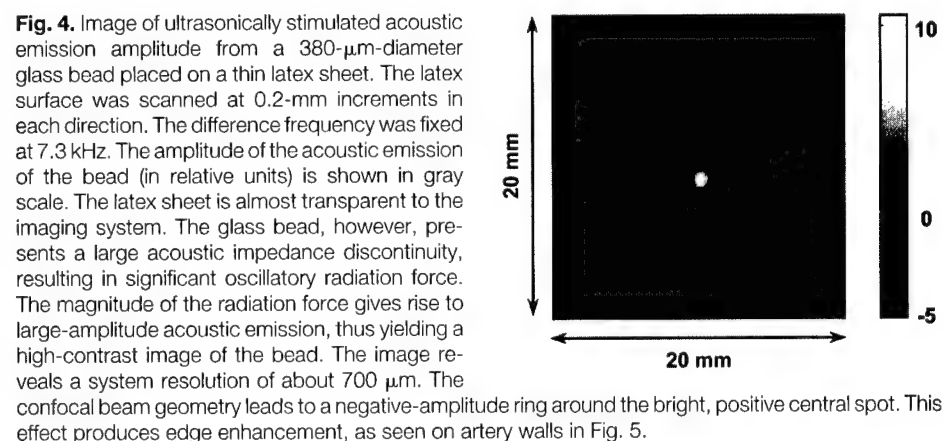


**Fig. 4.** Image of ultrasonically stimulated acoustic emission amplitude from a 380- $\mu$ m-diameter glass bead placed on a thin latex sheet. The latex surface was scanned at 0.2-mm increments in each direction. The difference frequency was fixed at 7.3 kHz. The amplitude of the acoustic emission of the bead (in relative units) is shown in gray scale. The latex sheet is almost transparent to the imaging system. The glass bead, however, presents a large acoustic impedance discontinuity, resulting in significant oscillatory radiation force. The magnitude of the radiation force gives rise to large-amplitude acoustic emission, thus yielding a high-contrast image of the bead. The image reveals a system resolution of about 700  $\mu$ m. The confocal beam geometry leads to a negative-amplitude ring around the bright, positive central spot. This effect produces edge enhancement, as seen on artery walls in Fig. 5.

Calcifications within the arteries produced distinctive amplitude and phase values when compared to the normal arterial walls (Fig. 5). The phase of the oscillation of driven mechanical systems relative to the driving force depends on the ratio of mass to stiffness (14). Calcified regions of the diseased artery, identified by an x-ray of the sample, produced phase shifts in acoustic emission completely different from that of the noncalcified, and thus softer or less dense, regions. The amplitude images are highly detailed and exhibit variations in acoustic emission from both calcified and uncalcified regions of the diseased artery. These differences are caused by variations in the product of the reflection properties  $d_r$  and the effective mechanical vibration admittance properties  $Q(\Delta\omega)$  of the tissue. Thus, vibro-acoustic spectrography is similar to conventional pulse-echo ultrasound imaging, which is sensitive to the ultrasonic parameters of the object, but has the advantage of also being sensitive to the mechanical admittance  $Q(\Delta\omega)$  at low frequencies.

Motion induced by ultrasound and measured with ultrasound pulse echo has been used previously to study "hardness" (15). However, the sensitivity of ultrasound pulse

echo to motion at common ultrasound frequencies is limited to several micrometers. The advantage of ultrasound-stimulated vibro-acoustic emission is its high displacement sensitivity. Cyclic displacement of 100 nm at 10-kHz produces an acoustic intensity of about  $3.0 \times 10^{-3} \text{ W/cm}^2$ . Hydrophones similar to the one used in these experiments are sensitive to as little as  $10^{-15} \text{ W/cm}^2$  and, therefore, can detect very small cyclic displacements. For example, the hydrophone detected an acoustic pressure of about  $15 \times 10^{-3} \text{ Pa}$  at a distance of 5 cm from the glass bead shown in Fig. 4. Under the assumption of isotropic vibration, this pressure would be produced by a similarly sized sphere vibrating with a displacement amplitude of about 6 nm. The method will be more sensitive for higher frequency sound because acoustic power is proportional to the square of frequency for constant displacement amplitude. The practical upper limits for the difference frequency produced with modern ultrasound transducers is about equal to their bandwidth. For modern transducers, this value is 80% or more of the central frequency of the transducer. For experiments like those we conducted, emission frequency well in excess of 1 MHz could be produced. The lower limit on the frequency of radiation pressure is zero, that is, static pressure.

Ultrasound-stimulated vibro-acoustic spectrography has potential applications in at least two general areas. The first is nondestructive evaluation of materials, where material characteristics and structural flaws can be identified by measuring changes in the mechanical response to vibration at a point. The object under test could be remotely vibrated, for instance, by beams propagating and interfering in either water or air, or beams propagating within the object could be used to produce acoustic emission from flaws. For medical imaging and detection, the technique appears particularly suitable for noninvasive detection of hard tissue inclusions, such as the imaging of arteries with calcification, detection of breast microcalcifications, visualization of hard tumors, and detection of foreign objects. The stiffness of soft tissues is related to their composition (for example, relative values of fibrotic content), and its change is often related to pathology or therapy. In conventional palpation, physicians estimate tissue stiffness by feeling with the fingers. Because changes of stiffness alter the vibration frequency response or damping of tissue, the present method can potentially provide a noninvasive, remote, high-resolution "palpation" technique that can reach small abnormalities that are otherwise untouchable by conventional methods.

## REFERENCES AND NOTES

1. J. Maynard, *Phys. Today* **49**, 26 (January 1996).
2. R. Muthupillai *et al.*, *Science* **269**, 1854 (1995).
3. For a review of elasticity imaging methods, see L. Gao, K. J. Parker, R. M. Lerner, S. F. Levinson, *Ultrasound Med. Biol.* **22**, 959 (1996).
4. The study of radiation force and radiation pressure dates back nearly one century, to the time of Rayleigh [Lord Rayleigh, *Philos. Mag.* **3**, 338 (1902); *ibid.* **10**, 364 (1905)]. More recent analysis of the theory and explanation of the physical significance of the mathematics can be found in G. R. Torr, *Am. J. Phys.* **52**, 402 (1984). Critical and historical reviews on radiation force and radiation pressure are presented in B.-T. Chu and R. E. Apfel, *J. Acoust. Soc. Am.* **72**, 1673 (1982) and R. E. Beyer, *ibid.* **63**, 1025 (1978). Some recent analysis of radiation force and pressure in attenuating medium (which may be applicable to biological tissues) are presented in O. V. Rudenko, A. P. Sarvazyan, S. Y. Emelianov, *J. Acoust. Soc. Am.* **99**, 2791 (1996) and Z.-Y. Jiang and J. F. Greenleaf, *ibid.* **100**, 741 (1996).
5. P. J. Westervelt, *J. Acoust. Soc. Am.* **23**, 312 (1951).
6. The complex drag coefficient due to radiation pressure is defined for unit energy density of the incident wave and can be written as (5)
 
$$d_r = \frac{1}{s} (\Pi_a + \Pi_s - \gamma \cos \beta) - \frac{i}{s} \gamma \sin \beta \quad (4)$$
 where  $\Pi_a$  and  $\Pi_s$  are the total absorbed and scattered powers, respectively;  $\gamma$  is the scattered intensity ( $\pi_a$ ,  $\pi_s$ , and  $\gamma$  are expressed per unit incident intensity);  $\beta$  is the angle between the incident and scattered intensities;  $s$  is the projected area of the object; and  $dS$  is the area element. The real and imaginary parts represent the components of the force parallel and perpendicular to, respectively, the incident field momentum. In our treatment, we assume a planar object normal to the beam axis; hence,  $d_r$  is real, and the force has only a normal component to the object surface.
7. The term "acoustic emission" is used here to describe the acoustic field in response to a cyclic vibration of the object and should not be confused with similar terminology used in the field of nondestructive testing of materials or in opto-acoustic imaging context, where it is used to describe the acoustic field resulting from structural deformation, cracking, or thermal expansion of the object. We note a fundamental difference between the method we present and that of opto-acoustic imaging. In ultrasound-stimulated vibro-acoustic spectrography, the ultrasound energy is converted directly to low-frequency acoustic energy by the object, whereas the opto-acoustic method relies on the conversion of light energy to heat, causing acoustic emission in response to rapid thermal expansion of the object.
8. Modulation of a single beam with the use of a focused transducer driven by an amplitude-modulated signal results in a field that is not spatially confined, producing a radiation force on any object (including the transducer itself) that happens to be in the beam path. The use of two single-frequency beams is advantageous because field modulation occurs only in a confined region, the size of which is controlled by the intersection of the two beams.
9. We define the short-term time average of an arbitrary function of time  $f(t)$  around time instance  $t$  as
 
$$\langle f(t) \rangle_T = \frac{1}{T} \int_{-T/2}^{T/2} f(\tau - t) d\tau \quad (5)$$
 The long-term time average is obtained when  $T \rightarrow \infty$ . To compute the short-term time average of the acoustic energy density relevant to acoustic emission at  $\Delta\omega$ , we choose  $T$  longer than the ultrasound wave period but much shorter than the acoustic wave period, that is,  $2\pi/\omega_2 \ll T \ll 2\pi/\Delta\omega$ .
10. In Eq. 2,  $H(\Delta\omega)$  can be position-invariant if the geometry of the propagation medium remains unchanged during the scan. In our experiments, we minimized position dependency by fixing the position of the transducer relative to the hydrophone and moving, instead, the object in raster-scanning motion.
11. Changing  $\Delta\omega$  by shifting the frequency of the ultrasound

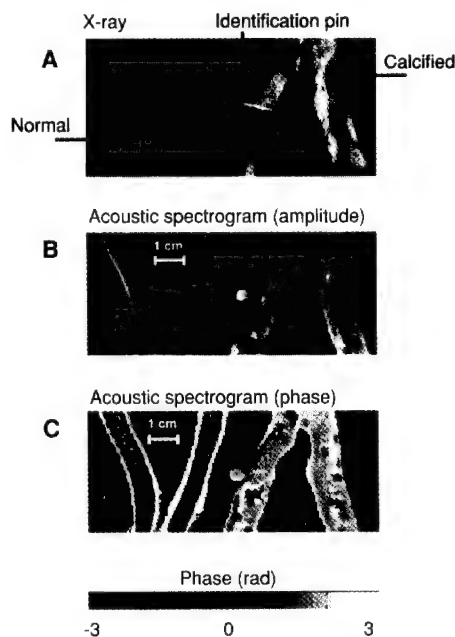


**Fig. 5.** Vibro-acoustic spectrography of excised human iliac arteries. **(A)** X-ray image of normal (left) and calcified (right) excised human iliac arteries obtained from a 35-year-old woman and a 67-year-old man, respectively. Bright areas indicate calcifications. **(B)** Vibro-acoustic spectrogram amplitude image at a fixed difference frequency of 6 kHz. Calcification details appear bright, whereas the arterial walls are dim. **(C)** Phase image. Calcified regions produce acoustic emission of different phase with respect to regions of the tissue having little calcification, as indicated by the x-ray.

beams does not change the beam amplitude because  $\Delta\omega$  is a small fraction of the bandwidth of typical ultrasound transducers. For instance, the bandwidth of the ultrasound transducer may be greater than 1 MHz, whereas  $\Delta\omega$  might be around 10 kHz.

12. M. R. Fisch, R. P. Moeller, E. F. Carome, *J. Acoust. Soc. Am.* **60**, 623 (1976).
13. D. R. Lide, Ed., *CRC Handbook of Chemistry and Physics* (CRC Press, Boca Raton, FL, ed. 72,

1991), pp. 6–158.

14. P. M. Morse and K. U. Ingard, *Theoretical Acoustics* (McGraw-Hill, New York, 1968).
15. T. Sugimoto, S. Ueha, K. Itoh, in *1990 IEEE Ultrasonics Symposium Proceedings*, B. R. McAvoy, Ed. (Institute of Electrical and Electronic Engineers, New York, 1990), vol. 3, p. 1377.

10 November 1997; accepted 17 February 1998

Major category: Physical Sciences; Minor category: Engineering

**Vibro-Acoustography: An Imaging Modality Based  
on Ultrasound-Stimulated Acoustic Emission**

Mostafa Fatemi and James F. Greenleaf

Ultrasound Research, Department of Physiology and Biophysics

Mayo Clinic and Foundation

Rochester, MN 55905

Correspondence author: Mostafa Fatemi, Ph.D., Ultrasound Research, Mayo Clinic, 200 First Street Southwest, Rochester, MN 55905; Tel: 507 284-0608, Fax: 507 266-0361, E-mail: fatemi.mostafa@mayo.edu

Number of text pages (including references and figure legends), of figures, and of tables: 29

Word and character counts: 6,171 words, 47,315 characters including spaces

Abbreviations footnote: List nonstandard abbreviations used five or more times. Define these where first mentioned in the text and do not use them in the title

Ultrasound-Stimulated Vibro-Acoustography (USVA)

Point Spread Function (PSF)

Data deposition footnote: Supply all database accession numbers and/or codes

**Abstract:** We describe theoretical principles of a new imaging modality that utilizes the acoustic response of an object to a highly localized dynamic radiation force of an ultrasound field. In this method, named Ultrasound-Stimulated Vibro-Acoustography (USVA), ultrasound is employed to exert a low-frequency (in kHz range) force on the object. In response, a portion of the object vibrates sinusoidally in a pattern determined by its viscoelastic properties. The acoustic emission field resulting from object vibration is detected and used to form an image that represents both the ultrasonic and low-frequency (kHz range) mechanical characteristics of the object. We report the relation between the emitted acoustic field and the incident ultrasonic pressure field in terms of object parameters. Also, we present the point spread function of the imaging system. The experimental images in this report have a resolution of about  $700\text{ }\mu\text{m}$ , high contrast, and high signal-to-noise ratio. USVA is sensitive enough to detect object motions on the order of nanometers. Possible applications include medical imaging and material evaluation.

## 1 INTRODUCTION

The study of objects in terms of their mechanical response to external forces is of considerable interest in material science and medical diagnosis. Elastic constants are closely connected to the thermodynamic properties of materials, and can be related to a wide range of physical parameters. Elastic constants, like spring constants, can be determined by measuring deformation in response to an applied force. Although a static force can be used for this purpose, using a dynamic force is preferred if one is interested in measuring the dynamic characteristics of the material [1].

Changes in elasticity of soft tissues are often related to pathology. Palpation is a traditional example of estimating mechanical parameters for tissue characterization, where a static force is applied and a crude estimation of the tissue elasticity is obtained through the sense of touch. In palpation, force is exerted on the body surface and the result is an accumulative response



of all the tissues below. Physicians can sense abnormalities if the response to palpation of the suspicious tissue is sufficiently different from that of normal tissue. However, if the abnormality lies deep in the body, or if it is too small to be resolved by touch, then the palpation method fails.

Elasticity imaging, a subject extensively investigated in recent years, is a quantitative method that measures the mechanical properties of tissue. The general approach is to measure tissue motion caused by an external (or, in some methods, internal) force/displacement and use it to reconstruct the elastic parameters of the tissue. Some investigators have used static force to compress the tissue and measured the resulting strain by ultrasound [2, 3]. Others have used external mechanical vibrators to vibrate the tissue and detected the resulting displacement in tissue by Doppler ultrasound [4–7]. For a review of elasticity imaging methods refer to [8]. A recently developed method employs an actuator to vibrate the body surface and then measures the strain waves with phase sensitive Magnetic Resonance Imaging [9].

Most of the elasticity imaging methods are based on an external source of force resulting in a spatially wide stress field distribution. This requires the stress field to pass through the superficial portion of an object before reaching the interior part. Analysis of the object response can be complicated because the stress field pattern changes, often unpredictably, at different depths before it reaches the region of interest within the object. An alternative strategy is to apply a localized stress directly in the region of interest. One way to accomplish this is to use the radiation pressure of an ultrasound source(s). Based on this strategy, Sugimoto, et al. [10] presented a method to measure tissue hardness using the radiation force of a single focused ultrasound beam. In this method, impulsive radiation force was used to generate localized deformation of the tissue. Resulting transient deformation was measured as a function of time by an ultrasound Doppler method. Radiation force has also been used to generate shear elastic

waves in tissues [11].

In this paper, we describe the principles of an imaging technique that produces a map of the mechanical response of an object to a force applied at each point. The method utilizes ultrasound radiation force to remotely exert a localized oscillating stress field at a desired frequency within (or on the surface of) an object. In response to this force, a part of the object vibrates. The size of this part and the motion pattern depends on object viscoelastic characteristics. The acoustic field resulting from object vibration, which we refer to as "acoustic emissions,"<sup>1</sup> is detected by a sensitive hydrophone and used to form the image of the object. This method benefits from the high spatial definition of ultrasound radiation force and high motion detection sensitivity offered by the hydrophone. We call this technique "ultrasound-stimulated vibro-acoustography" (USVA). Some general aspects of this method including some experimental results have been outlined by the authors in [12]. Here, we present the theoretical foundations of USVA.

## 2 METHODS

Our aim is to image an object based on its mechanical characteristics. This is achieved by vibrating the object by applying a highly localized oscillating force to each point of the object. The localized force is produced by modulating the intensity, and thereby the radiation force, of the ultrasound at low frequencies (normally in kHz range). The resulting sound emitted by the object is a function of object mechanical characteristics and the location of the excitation point. The image is produced by mapping the amplitude or phase of this sound, which is detected by a sensitive hydrophone, versus position. Figure 1 illustrates this method. In the following section we describe the relationship between the USVA image and the properties of the object.

---

<sup>1</sup> The term "acoustic emission" is used to describe the acoustic field in response to a cyclic vibration of the object. Similar terminology is also used in the field of nondestructive testing of materials and in opto-acoustic imaging to describe a different phenomenon, usually the acoustic field resulting from structural deformation.

### 3 THEORY

#### Generation of a dynamic radiation force on a target

The acoustic radiation force is the time average force exerted by an acoustic field on an object. This force is an example of a universal phenomenon in any wave motion that introduces some type of unidirectional force on absorbing or reflecting targets in the wave path. Radiation force is produced by a change in the energy density of an incident acoustic field. For a review of this phenomenon refer to [13]. Consider a plane ultrasound beam interacting with a planar object of zero thickness and arbitrary shape and boundary impedance that scatters and absorbs. The radiation force vector,  $\mathbf{F}$ , arising from this interaction has a component in the beam direction and another transverse to it. The magnitude of this force, is proportional to the average energy density of the incident wave  $\langle E \rangle$  at the object, where  $\langle \rangle$  represents the time average, and  $S$ , the area of the projected portion of the object [14]

$$\mathbf{F} = \mathbf{d}_r S \langle E \rangle, \quad (1)$$

where  $\mathbf{d}_r$  is the vector drag coefficient with a component in the incident beam direction and another transverse to it. The coefficient  $\mathbf{d}_r$  is defined per unit incident energy density and unit projected area. For a planar object,  $\mathbf{d}_r$  is numerically equal to the force on the object. Physically, the drag coefficient represents the scattering and absorbing properties of the object and is given by [14]

$$\mathbf{d}_r = \hat{\mathbf{p}} \frac{1}{S} \left( \Pi_a + \Pi_s - \int \gamma \cos \alpha_s dS \right) + \hat{\mathbf{q}} \frac{1}{S} \int \gamma \sin \alpha_s dS, \quad (2)$$

where  $\hat{\mathbf{p}}$  and  $\hat{\mathbf{q}}$  are the unit vectors in the beam direction and normal to it, respectively. The quantities  $\Pi_a$  and  $\Pi_s$  are the total absorbed and scattered powers, respectively, and  $\gamma$  is the scattered intensity, all expressed per unit incident intensity. Also,  $\alpha_s$  is the angle between the

incident and the scattered intensity, and  $dS$  is the area element. The drag coefficient can also be interpreted as the ratio of the radiation force magnitude on a given object to the corresponding value if the object were replaced by a totally absorbing object of similar size. This is because  $|d_r| = 1$  for a totally absorbing object. This coefficient can be determined for objects of different shapes and sizes. For simplicity, we assume a planar object normal to the beam axis. In this case, the transverse component vanishes, thus, the drag coefficient (force) will have only a component normal to the target surface which we denote by scalar  $d_r$  ( $F$ ). Values of  $d_r$  for spheres, in terms of the diameter and the wavelength, are given in [14].

To produce a dynamic radiation force, one can use an amplitude modulated beam [15]. Consider an amplitude modulated incident (ultrasonic) pressure field,  $p(t)$ , as

$$p(t) = P_{\omega_0} \cos(\Delta\omega t/2) \cos \omega_0 t, \quad (3)$$

where  $P_{\omega_0}$ ,  $\Delta\omega/2$ , and  $\omega_0$  are the pressure amplitude, modulating frequency, and the center frequency, respectively. In our analysis and experiments, we assume that the condition  $\Delta\omega \ll \omega_0$  holds. In such a case, the energy density of the incident field has slow variations in time. To discriminate the slow time variations of a function, let us define the *short-term time average* of an arbitrary function  $\xi(t)$  over the interval of  $T$  seconds at time instance  $t$ , as  $\langle \xi(t) \rangle_T = \frac{1}{T} \int_{t-T/2}^{t+T/2} \xi(\tau) d\tau$ , which is a function of  $t$ . The long-term time average (or simply, the time average) is obtained by setting  $T \rightarrow \infty$ . To compute the short-term time average of the acoustic energy density relevant to field variations at  $\Delta\omega/2$ , we choose  $T$  longer than the ultrasound wave period but much shorter than the modulation period, that is  $2\pi/\omega_0 \ll T \ll 4\pi/\Delta\omega$ . Under this condition, the short-term time average of  $p^2(t)$  is  $\langle p^2(t) \rangle_T = \frac{P_{\omega_0}^2}{4} (1 + \cos \Delta\omega t)$ . The energy density is given by  $p^2(t)/\rho c^2$  where  $\rho$  and  $c$  are the density and propagation speed in the medium [16]. We are interested in the time-varying

component of the short-term time average of the energy density. Denoting this component by  $e_{\Delta\omega}(t)$ , we can write:  $e_{\Delta\omega}(t) = \frac{P_{\omega_0}^2}{4\rho c^2} \cos \Delta\omega t$ . This component of the energy density produces a time varying radiation force on the target (Eq. 1) at frequency  $\Delta\omega$ . The amplitude of this force,  $F_{\Delta\omega}$ , is

$$F_{\Delta\omega} = \frac{P_{\omega_0}^2}{4\rho c^2} S d_r. \quad (4)$$

This equation states that the time-varying force amplitude is proportional to the square of incident ultrasound pressure, or equivalently, to the incident power. If the object moves in response to this force, then the high-frequency ultrasound energy would convert to low-frequency mechanical energy.

#### Acoustic emission from a target due to a dynamic force

The radiation force  $F_{\Delta\omega}$  vibrates the target object at frequency  $\Delta\omega$ . Object vibration results in an acoustic field in the medium (acoustic emission). This field is related to object shape, size, and viscoelastic properties. To present a conclusive analysis of this relationship, we have to assume an object with specific characteristics. Here, we assume that the vibrating object has a circular cross section of radius  $b$  and uniformly vibrates back and forth like a piston. This choice allows us to illustrate the concept in a simple form. We also consider an area  $S \leq \pi b^2$  of the piston surface to be projected normally by the beam. Similar solutions can be carried out for other objects.<sup>2</sup>

The steady state normal velocity amplitude of a piston,  $U_{\Delta\omega}$ , due to a harmonic force  $F_{\Delta\omega}$  at frequency  $\Delta\omega$ , can be described in terms of the mechanical impedance  $Z_{\Delta\omega}$ ,

$$U_{\Delta\omega} = \frac{F_{\Delta\omega}}{Z_{\Delta\omega}}, \quad (5)$$

---

<sup>2</sup> The theory can be extended to include arbitrary vibrating-part shapes and nonuniform displacement of the object. Nonuniform displacement would be an important issue when the vibration wavelength in the object material is smaller than  $2b$ .

where  $Z_{\Delta\omega} = Z'_m + Z_r$  is comprised of the mechanical impedance of the object in vacuum  $Z'_m$ , and the radiation impedance of the object  $Z_r$ , all defined at  $\Delta\omega$ . Modeling the object as a mass-spring system,  $Z'_m$  can be written in terms of  $\Delta\omega$  as [16, 17]

$$Z'_m = R'_m - j \left( m\Delta\omega - \frac{K'}{\Delta\omega} \right), \quad (6)$$

where  $m$ ,  $R'_m$ , and  $K'$  are the mass, mechanical resistance, and the spring constants of the object, respectively. The radiation impedance of the piston can be written as [17]

$$Z_r = \pi b^2 (R_r - jX_r), \quad (7)$$

where

$$R_r = \rho c \left[ 1 - \frac{c}{\Delta\omega b} J_1 \left( \frac{c}{2\Delta\omega b} \right) \right], \quad (8)$$

and

$$X_r = \frac{4\rho c}{\pi} \int_0^{\frac{\pi}{2}} \sin \left( \frac{2\Delta\omega b}{c} \cos \alpha \right) \sin^2 \alpha d\alpha, \quad (9)$$

where  $J_1(\cdot)$  is the first-order Bessel function of the first kind. In many applications of our interest, the wavelength is much greater than the object size, hence,  $\frac{\Delta\omega}{c}b \rightarrow 0$ . In such cases  $Z_r$  assumes a simpler form:

$$Z_r = \pi b^3 \rho \Delta\omega \left( \frac{\Delta\omega b}{2c} - j \frac{8}{3\pi} \right). \quad (10)$$

The mechanical impedance of the piston object can now be written as

$$\begin{aligned} Z_{\Delta\omega} &= (R'_m + \pi b^2 R_r) - j \left( m\Delta\omega - \frac{K'}{\Delta\omega} + \pi b^2 X_r \right) \\ &\approx \left( R'_m + \frac{\pi \rho}{2c} b^4 \Delta\omega^2 \right) - j \left( m\Delta\omega - \frac{K'}{\Delta\omega} + \frac{8}{3} \rho b^3 \Delta\omega \right), \quad \frac{\Delta\omega b}{c} \rightarrow 0. \end{aligned} \quad (11)$$

Once we calculate  $U_{\Delta\omega}$ , we can calculate the pressure field it produces in the medium. We assume that the acoustic emission signal propagates in a free and homogenous medium. The

farfield acoustic pressure due to a piston source of radius  $b$  set in a planar boundary of infinite extent is given by [17],

$$P_{\Delta\omega} = -j\Delta\omega\rho \frac{\exp(j\Delta\omega l/c)}{4\pi l} \left[ \frac{2J_1\left(\frac{\Delta\omega b}{c} \sin \vartheta\right)}{\frac{\Delta\omega b}{c} \sin \vartheta} \times \frac{\cos \vartheta}{\cos \vartheta + \beta_B} \right] (2\pi b^2 U_{\Delta\omega}), \quad (12)$$

where  $l$  is the distance from the observation point to the center of the piston,  $\vartheta$  is the angle between this line and the piston axis, and  $\beta_B$  is the specific acoustic admittance of the boundary surface.<sup>3</sup> The factor of two comes from the presence of the boundary wall. It would be replaced by unity if the boundary wall were not present [16]. The acoustic emission field resulting from object vibration can be written in terms of the incident ultrasound pressure by combining Eqs. 4, 5, and 12, as

$$P_{\Delta\omega} = \left\{ j \frac{\Delta\omega}{c^2} \times \frac{\exp(j\Delta\omega l/c)}{4\pi l} \left[ \frac{2J_1\left(\frac{\Delta\omega b}{c} \sin \vartheta\right)}{\frac{\Delta\omega b}{c} \sin \vartheta} \times \frac{\cos \vartheta}{\cos \vartheta + \beta_B} \right] \right\} \times \left[ \frac{1}{(R'_m + \pi b^2 R_r) - j(m\Delta\omega - \frac{K'}{\Delta\omega} + \pi b^2 X_r)} \right] (2\pi b^2) P_{\omega_0}^2 S d_r, \quad (13)$$

For wavelengths long compared to the object size, i.e., when  $b\Delta\omega/c \rightarrow 0$ , the term in the first brace approaches a constant, hence we may consider the contents of the first brace to be an object independent function (the specific acoustic admittance  $\beta_B$  relates to the surrounding boundary surface). Under these conditions, the first brace in the above equation represents the effect of the medium on the acoustic emission field, which we may call the *medium transfer function*, and denote it by

$$H_{\Delta\omega}(l) = j \frac{\Delta\omega}{c^2} \times \frac{\exp(j\Delta\omega l/c)}{4\pi l} \left[ \frac{2J_1\left(\frac{\Delta\omega b}{c} \sin \vartheta\right)}{\frac{\Delta\omega b}{c} \sin \vartheta} \times \frac{\cos \vartheta}{\cos \vartheta + \beta_B} \right]. \quad (14)$$

<sup>3</sup> The specific acoustic admittance is  $\beta_B = \frac{\rho c}{Z_B}$ , where  $Z_B$ , the acoustic impedance of the boundary, represents the ratio between the pressure and normal fluid velocity at a point on the surface.

The second bracket in Eq. 13 is  $\frac{1}{Z_{\Delta\omega}}$ , or the mechanical admittance of the object at the frequency of the acoustic emission ( $\Delta\omega$ ), and we denote it by  $Y_{\Delta\omega}$ . It is convenient to combine this term with the next term ( $2\pi b^2$ ) in Eq. 13, as  $Q_{\Delta\omega} = 2\pi b^2 Y_{\Delta\omega} = 2\pi b^2 / Z_{\Delta\omega}$ , which is the total acoustic outflow<sup>4</sup> by the object per unit force. Function  $Q_{\Delta\omega}$  represents the object characteristics at the acoustic frequency. We may thus rewrite Eq. 13 in a more compact form as

$$P_{\Delta\omega} = H_{\Delta\omega}(l) Q_{\Delta\omega} P_{\omega_0}^2 S d_r. \quad (15)$$

Equation 15 indicates that the acoustic emission pressure is proportional to: 1) the square of ultrasound pressure  $P_{\omega_0}$ , 2) the ultrasound characteristics of the object,  $d_r$ , in the projected area  $S$ , 3) the acoustic outflow by this object,  $Q_{\Delta\omega}$ , representing the object size  $b$  and its mechanical admittance at the acoustic frequency,  $Y_{\Delta\omega}$ , and 4) the transfer function of the medium at the acoustic frequency,  $H_{\Delta\omega}(l)$ . The above equation illustrates the basic nonlinear relationship between the ultrasound and acoustic emission pressure amplitudes. Note that neither the medium nor the object need to be nonlinear for this relationship to hold. It is interesting to note that the projection area  $S$ , and the vibrating area  $\pi b^2$  play different roles. The projection area determines the extent of the force applied to the object (Eq. 4). The vibrating area, however, influences the total acoustic outflow in the medium caused by object vibration. The mechanism of object vibration is somewhat analogous to that of a loudspeaker, where the electromotive force is exerted to a small area of the membrane (usually at the center) causing the entire membrane surface to vibrate. In our method, the size of the vibrating area depends on the object structure. For a free suspended point object, smaller than the beam cross section, the vibrating area would be the same as the projection area. For a large stiff plate, however, the vibrating area could

---

<sup>4</sup> Acoustic outflow is the volume of the medium (e.g., the fluid) in front of the object surface that is displaced per unit time due to object vibration.



be much larger than the projected area (similar to a loudspeaker). In some cases it is more convenient to have the acoustic emission field in terms of the applied force  $F_{\Delta\omega}$ . Referring to Eq. 4, we can rewrite Eq. 15 as

$$P_{\Delta\omega} = 4\rho c^2 H_{\Delta\omega}(l) Q_{\Delta\omega} F_{\Delta\omega}. \quad (16)$$

Again in analogy to a loudspeaker,  $F_{\Delta\omega}$ ,  $Q_{\Delta\omega}$ , and  $H_{\Delta\omega}(l)$  represent the electromotive force, dynamic characteristics of the membrane, and the propagation medium transfer function.

### Beam forming

To probe an object with the dynamic radiation force at high-spatial resolution, it is ideal to confine the dynamic stress field to a very small region in three-dimensional space. We may define the resolution cell of the system as the volume within which the amplitude of the modulated field is high enough to produce a stress field on a target. The purpose of beam forming is to produce a resolution cell as small as possible. An amplitude modulated single-focused beam can provide a resolution cell that is small in diameter but long in the depth direction. A superior strategy that can achieve small resolution cell in all dimensions is to use two unmodulated focused beams at slightly different frequencies, and allow them to cross each other at their focal regions. This is accomplished by projecting two coaxial, confocal, continuous wave (CW) ultrasound beams on the object. An amplitude modulated field is produced only at the interference region of the two unmodulated beams around their focal areas, resulting in a small resolution cell. For this purpose, elements of a two-element spherically focused annular array (consisting of a central disc with radius  $a_1$  and an outer ring with the inner radius of  $a'_2$  and outer radius of  $a_2$ ) are excited by separate CW signals at frequencies  $\omega_1 = \omega_0 - \Delta\omega/2$  and  $\omega_2 = \omega_0 + \Delta\omega/2$ . We assume that the beams are propagating in a lossless medium, in the  $+z$  direction of a Cartesian coordinate system  $(x, y, z)$ , with the joint focal point at  $z = 0$ . The resultant pressure field on

the  $z = 0$  plane may be written as

$$p(t) = P_1(r) \cos(\omega_1 t + \psi_1(r)) + P_2(r) \cos(\omega_2 t + \psi_2(r)), \quad (17)$$

where  $r = \sqrt{x^2 + y^2}$  is the radial distance. The amplitude functions are [16, 18]

$$P_1(r) = \rho c U_{01} \frac{\pi a_1^2}{\lambda_1 z_0} \text{jinc}\left(\frac{r a_1}{\lambda_1 z_0}\right), \quad (18)$$

and

$$P_2(r) = \rho c U_{02} \frac{\pi}{\lambda_2 z_0} \left[ a_2^2 \text{jinc}\left(\frac{r a_2}{\lambda_2 z_0}\right) - a_2'^2 \text{jinc}\left(\frac{r a_2'}{\lambda_2 z_0}\right) \right], \quad (19)$$

where  $\lambda_i = 2\pi/\omega_i$ ,  $i=1, 2$ , is the ultrasound wavelength,  $U_{0i}$  is the particle velocity amplitude at the  $i$ -th transducer element surface, and  $\text{jinc}(X) = J_1(2\pi X)/\pi X$ . The phase functions,  $\psi_i(r) = -\frac{\pi r^2}{\lambda_i z_0}$ , for  $i=1, 2$ , are conveniently set to be zero at the origin.

Now, we define a *unit point target* at position  $(x_0, y_0)$  on the focal plane with a drag coefficient distribution as

$$d_r(x, y) = \delta(x - x_0, y - y_0), \quad (20)$$

such that  $d_r(x, y) dx dy$  is unity at the  $(x_0, y_0)$  and zero elsewhere. This equation is merely used as a mathematical model because  $d_r$  is physically finite. In this case, the projected area can be considered to be  $S = dx dy$ . We replace  $d_r S$  in Eq. 1 with  $d_r(x, y) dx dy$ , and follow the steps similar to those outlined in Eqs. 3 and 4 for the pressure field expressed by Eq. 17, then the complex amplitude of the normal component of the force on the unit point target can be found as

$$F_{\Delta\omega}(x_0, y_0) = \frac{1}{4} \rho U_{01} U_{02} \frac{\pi a_1^2}{\lambda_1 z_0} \text{jinc}\left(\frac{r_0 a_1}{\lambda_1 z_0}\right) \left[ \frac{\pi a_2^2}{\lambda_2 z_0} \text{jinc}\left(\frac{r_0 a_2}{\lambda_2 z_0}\right) - \frac{\pi a_2'^2}{\lambda_2 z_0} \text{jinc}\left(\frac{r_0 a_2'}{\lambda_2 z_0}\right) \right] \times \exp\left(-j \frac{r_0^2 \Delta\omega}{2c z_0}\right), \quad (21)$$

where the arguments  $x_0$  and  $y_0$  are added to denote the position of the point target, and  $r_0 = \sqrt{x_0^2 + y_0^2}$ . Equation 21 describes the spatial distribution of the force (the stress field). This

equation shows that the stress field is confined to the regions near the beam axis ( $r_0 = 0$ ), and decays as the radial distance  $r_0$  increases. The lateral extent of the stress field, and hence the resolution cell diameter, would be smaller at higher ultrasound frequencies (smaller  $\lambda_1$  and  $\lambda_2$ ). One can calculate the total force on an arbitrary object by integrating the force over the projected area. The axial extent of the resolution cell (depth resolution, or the depth of field) can be determined by calculating the force  $F_{\Delta\omega}$  as a function of the depth variable, in a fashion as outlined in Eqs. 17 to 21. For conciseness, we will only present the measured values for the depth resolution in the Results section.

Loss in the propagation path would attenuate both ultrasound beams, thus less radiation force would be generated by the remaining ultrasound energy. In the case of soft tissues, the force attenuation factor is  $A(z_0) = \exp[\alpha z_0(\omega_1 + \omega_2)]$ , where  $\alpha$  is the attenuation coefficient of the tissue. Energy loss in the medium would also result in generation of a separate radiation stress on the medium along the ultrasound paths. However, since the two beams propagate along separate paths in the CW form, they exert mainly steady radiation stresses to the medium, which does not cause object or medium vibrations. Dynamic radiation force is produced only in the interference region around the focal area. This is another advantage of using two unmodulated beams over a modulated single beam.

### **Image formation**

To produce an image we scan the object in a plane and record the complex amplitude of the acoustic emission,  $P_{\Delta\omega}$ , at different positions. In this process, we keep  $\Delta\omega$  fixed. For transverse view images, the scan plane is the focal plane ( $x - y$ ). Alternatively, for the parallel view the scan plane is the  $x - z$  plane. In the conventional ultrasound imaging context, these two views are called the C-scan and B-scan, respectively. Our main focus here is the transverse

view imaging. In this case, the acoustic emission data obtained by vibrating the object at point  $(x, y)$  are assigned to the corresponding point  $(x, y)$  in the image.

Before defining the image, we need to define the function that represents the object. Referring to Eq. 15, the terms that are object dependent are the drag coefficient  $d_r$  and the function  $Q_{\Delta\omega}$  (assuming that  $H_{\Delta\omega}(l)$  is object independent). The object function  $g(x, y)$  is thus defined as the spatial distribution of these terms,

$$g(x, y) = Q_{\Delta\omega}(x, y)d_r(x, y). \quad (22)$$

Variables  $x$  and  $y$  are added to denote the dependency of  $d_r$  and  $Q_{\Delta\omega}$  on position. In particular,  $Q_{\Delta\omega}(x, y)$  implies the total acoustic outflow by the object when the force is applied at point  $(x, y)$ .

Commonly, an imaging system is studied through its point spread function (PSF), which is defined as the image of a point object. To determine the PSF of our system, we consider a unit point target at the origin with unit mechanical response,  $Q_{\Delta\omega}(x, y) = 1$ . Hence, referring to Eqs. 20 and 22, we can write  $g(x, y) = \delta(x, y)$ . To obtain the PSF, we move this point object to every possible position  $(x_0, y_0)$  on the  $z = 0$  plane and form the image using the resulting acoustic emission field,  $P_{\Delta\omega}(x_0, y_0)$ . Since  $x_0$  and  $y_0$  are now being treated as variables, we may replace them by variables  $x$  and  $y$ , respectively. We define the normalized PSF of the coherent imaging system as the complex function

$$h(x, y) = P_{\Delta\omega}(x, y)/P_{\Delta\omega}(0, 0). \quad (23)$$

Division by  $P_{\Delta\omega}(0, 0)$  cancels the constant multipliers. Referring to Eqs. 16 and 21, we can write

$$h(x, y) = \frac{1}{a_2^2 - a_2'^2} \text{jinc}\left(\frac{ra_1}{\lambda_1 z_0}\right) \left[ a_2^2 \text{jinc}\left(\frac{ra_2}{\lambda_2 z_0}\right) - a_2'^2 \text{jinc}\left(\frac{ra_2'}{\lambda_2 z_0}\right) \right] \exp\left(-j\frac{r^2 \Delta\omega}{2cz_0}\right). \quad (24)$$

This equation illustrates that the system PSF is a circularly symmetric function with the peak at the origin and decaying amplitude with increasing the radial distance  $r$ . Amplitude decays faster for higher ultrasound frequency. This function will be discussed further in the next section.

#### 4 EXPERIMENTS

The experimental setup is shown in Fig. 2. The confocal transducer is constructed using a spherical piezoelectric cap. The two elements are constructed by dividing the back electrode of the piezoelectric wafer into a central disc and the outer ring, such that the elements have identical beam axes and focal lengths. Radii of the elements are  $a_1=14.8$  mm,  $a_2=22.5$  mm, and  $a'_2=16.8$  mm, and the focal distance is 70 mm. Transducer elements were driven by two stable RF synthesizers (HP 33120A and Analogic 2045) at frequencies of  $f_0 - \Delta f/2$  and  $f_0 + \Delta f/2$ , where  $f_0=3$  MHz, and the value of  $\Delta f = \Delta\omega/2\pi$  is stated separately for each experiment. The object was placed at the focal plane of the ultrasound beams in a water tank. Sound produced by the object vibration was detected by an audio hydrophone (ITC model 680, sensitivity  $-154$  dB re  $1\text{V}/\mu\text{Pa}$ ) placed within the water tank. The received signal was filtered and amplified by a programmable filter (Stanford Research Systems, SR650) to reject noise, then digitized by a 12 bits/sample digitizer (HP, E1429A) at a rate sufficiently higher than the Nyquist rate for the particular  $\Delta f$  used. Data were recorded on a computer disc (Sun Sparc computer). For coherent imaging, which requires the phase information, the reference signal (i.e.,  $\cos \Delta\omega t$ ) was obtained by electronic down mixing of the two driving signals and was recorded along with the hydrophone signal. The relative phase of the acoustic emission data was then calculated at each point by discrete Hilbert transform. We conducted two experiments. The first experiment is designed to verify the relationship between the acoustic emission pressure and the ultrasound pressure (Eq. 15), and the second is designed to experimentally measure the point spread function

stated in Eq. 24. These experiments are presented to prove the principles of the method. Further experiments, illustrating applications of the method for evaluation of object mechanical properties and tissue imaging, are presented in [12].

## 5 RESULTS

### Acoustic emission versus ultrasound pressure

Equation 15 states that the acoustic emission field amplitude is linearly proportional to the square of the incident ultrasound pressure, or equivalently, to the incident power. To test this hypothesis, a calibrated 1 mm diameter ultrasound needle hydrophone, with its tip facing the ultrasound beam, was used to measure the ultrasound field at the focal point. (This is in addition to the audio hydrophone.) The tip of the hydrophone also served as an object to generate the acoustic emission. Here,  $\Delta f$  was set at 40 kHz, and the radial distance from the tip of the needle hydrophone to the audio hydrophone was about 65 mm. The result is shown in Fig. 3. The slope of the acoustic emission intensity versus ultrasonic intensity indicates that the intensity of the acoustic emission field is proportional to the square of the ultrasound intensity, or equivalently, the acoustic emission pressure amplitude is linearly proportional to the ultrasound power, as predicted by Eq. 15. In another experiment, a 450  $\mu\text{m}$  diameter glass bead was used as a point object. In this case,  $\Delta f$  was set at either 7 or 40 kHz. The radial distance from the glass bead to the audio hydrophone was about 50 mm. Again, the data indicate a quadratic relationship between the acoustic emission and ultrasonic intensities. These glass bead data also show that increasing the frequency increases the acoustic intensity. This can be better understood by investigating the theoretical model presented in Eq. 13. If we assume that the mechanical admittance of the object is approximately constant at these frequencies, then the object behaves almost as a point source and the acoustic pressure amplitude is proportional to  $\Delta\omega$ . Hence,

the acoustic emission intensities  $I_{\Delta\omega_1}$  and  $I_{\Delta\omega_2}$  at frequencies  $\Delta\omega_1$  and  $\Delta\omega_2$ , respectively, are related by  $I_{\Delta\omega_2}/I_{\Delta\omega_1} = (\Delta\omega_2/\Delta\omega_1)^2$ . Now, letting  $\Delta\omega_1$  and  $\Delta\omega_2$  correspond to 7 and 40 kHz, respectively, we can write the intensity ratio as:  $[I_{\Delta\omega_2}/I_{\Delta\omega_1}]_{\text{dB}} = 20 \log (\Delta\omega_2/\Delta\omega_1) = 15 \text{ dB}$ . The mean value of the intensity ratio calculated from the glass bead data at 7 and 40 kHz is 16 dB, which is in close agreement with the theoretical result.

## PSF Measurement

To demonstrate the image formation process and support the theoretical derivation of the PSF (Eq. 24), we evaluated this function experimentally. For this purpose, we used a 380  $\mu\text{m}$  diameter glass bead as a model for a point and placed it on a thin latex sheet. The latex sheet produces only a small change in the incident energy, and hence, does not produce significant radiation force or acoustic emission. The entire object was placed in a water tank and the latex sheet surface was scanned in a raster format at 0.2 mm increments in either direction at  $\Delta f = 7.3 \text{ kHz}$ . The amplitude and phase of the acoustic emission signal were calculated at each point relative to the reference signal data. The phase was normalized to the phase value at the center of the bead. The resulting in-phase, quadrature, phase, and magnitude images are shown in Figs. 4a through d. Transverse image resolution, defined as the -6dB width of the bead image, is approximately 700  $\mu\text{m}$  for the in-phase image in either dimension (refer to Fig. 5). To compare the experimental results with those of the theory, we calculated the profile of the PSF, for the transducer parameters used in this experiment, according to Eq. 24. Figure 5 shows the theoretical PSF profile and the glass bead profile obtained from the experiment (in-phase image profile, shifted to center at zero). This figure shows excellent agreement between theory and experiment for amplitudes above 20% of the peak. The experimental data show some background offset about 12% of the peak. We believe that this background offset is caused at least by the

following sources: 1) acoustic emission by the latex sheet, 2) the background acoustic noise in the experimental setup caused by equipment fans and some structural and building vibrations, 3) nonlinearity of water which can produce a nonlinear mix of the two beams even in the absence of the object, and 4) streaming as a result of energy absorption by water [14] which in turn can vibrate the latex sheet blocking the stream. To evaluate the depth resolution (or the slice thickness), we placed the glass bead on the beam axis and scanned it in the z-direction about the focal point. The depth resolution, defined as the distance between the points where the amplitude of the acoustic emission field drops to  $-6$  dB of its peak, was 9 mm.

## 6 DISCUSSION

### System properties

*Spectral Characteristics*—In general, USVA images represent object characteristics at two ends of the spectrum: the drag coefficient at the ultrasound frequency, and the mechanical admittance at the low acoustic frequency  $\Delta f$ . The ultrasound frequency is usually set at a value suitable to form the beam, while  $\Delta f$  can vary in a wide range depending on the application. If the two beams are produced by similar ultrasound transducer elements, then the practical upper limit for  $\Delta f$  is about equal to the transducer bandwidth. The lower limit of  $\Delta f$  is zero.

*Sensitivity*—System sensitivity in detecting very small displacements is an important practical issue, especially when the allowable ultrasound power is limited (for example, in medical imaging). Motion measurement with ultrasound pulse echo has been used previously to study “stiffness” of tissues [10]. However, the sensitivity of ultrasound pulse echo to motion, at common medical ultrasound frequencies, is limited to several micrometers. An advantage of USVA is its high displacement sensitivity. Cyclic displacement of 100 nanometers at 10 kHz produces an acoustic intensity of about  $3.0 \times 10^{-3}$  watts/cm<sup>2</sup>. Hydrophones similar to the one



used in these experiments are sensitive to as little as  $10^{-15}$  watts/cm<sup>2</sup>, and therefore, are capable of detecting very small cyclic displacements. For instance, the hydrophone detected an acoustic pressure of about  $15 \times 10^{-3}$  Pascals at a distance of 5 cm from the glass bead shown in Fig. 4. Under assumptions of isotropic vibration, this pressure would be produced by a similar sized sphere vibrating with a displacement amplitude of about 6 nm. Sensitivity increases at higher frequencies because the acoustic emission pressure is proportional to frequency for constant mechanical admittance (Eq. 13).

*Comparisons with pulse-echo systems*—Some contrasting features of USVA with respect to the conventional ultrasound pulse-echo imaging (B-mode and C-mode) are:

1. A pulse-echo image represents object microstructure by displaying its ultrasonic reflectivity distribution. The acoustic emission signal in a USVA system is proportional to the drag coefficient  $d_r(x, y)$ , which is a local ultrasound parameter, and to the function  $Q_{\Delta\omega}(x, y)$ , which represents the bulk response of the object at acoustic frequency  $\Delta\omega$ . Hence, a USVA image, in general, represents both the microstructure and macrostructure of the object.
2. The echo signal in a pulse-echo system is a linear function of the incident ultrasound pressure amplitude and the amplitude reflection coefficient of the object. In USVA, however, the acoustic emission signal is proportional to the ultrasound *power* and the *power* reflection coefficient of the object.
3. Pulse-echo systems are not directly sensitive to medium absorption. Absorption is indicated as relative changes in the amplitude of the echoes resulting from the scatterers within the medium. In a USVA system, the acoustic emission can be produced directly as a result of energy absorption by the medium, even if the medium is homogeneous (refer to Eq. 2).
4. Pulse-echo systems are generally broadband. The USVA method presented here is basically

a narrowband technique.

5. Pulse echo systems achieve high depth resolution by transmitting short wideband pulses. A USVA system gains its depth resolution by tailoring beam geometry to limit the depth of the region where the two beams interfere. A USVA system does not require a wide bandwidth signal to achieve a high depth resolution.
6. The data of USVA images are acquired one point at a time, which resembles the data acquisition in C-mode pulse-echo systems. B-mode pulse-echo systems, however, require much less acquisition time because the data are collected one line at a time.

### Applications

The method presented here promises applications in two general areas: medical imaging and material evaluation.

*Medical Applications*—USVA can be used to image tissues and evaluate their mechanical characteristics. To employ USVA for *in vivo* applications, one must take into account limitations such as safe (ultrasound) power limit, tissue attenuation, body noise, and phase aberration. The required ultrasound power to generate a detectable acoustic emission depends on the object, acoustic noise, and the receiver sensitivity. Experimental results shown in Fig. 3 demonstrate that ultrasound intensities as low as  $30 \text{ mW/cm}^2$  are sufficient to detect the acoustic emission from a 1 mm diameter object with our hydrophone in the water tank. This power value is much smaller than the FDA limit for safe diagnostic ultrasound applications. Tissue attenuation reduces the ultrasound intensity at the target, and hence, the acoustic emission (by the factor  $A(z_0)$ ). Attenuation limits the usable ultrasound frequency, and hence, lowers the resolution. It also limits the signal-to-noise-ratio (SNR) because of the loss in the acoustic emission energy as a result of ultrasound attenuation by tissue. Direct effect of tissue attenuation on the acoustic emission

signal is probably negligible because attenuation of the compressional waves at frequencies in the order of a few kHz in soft tissues is low. Sources of biological noise of the human body include cardiovascular and respiratory systems, and muscle movements. Body noise is usually concentrated below 1 KHz and can be filtered out if  $\Delta f$  is above this value. The SNR can be improved by increasing the time duration of the signal recorded at each point (to increase the signal energy) and using very narrow band filters (to reject the noise), while keeping the ultrasound power within the safe level. Phase aberration in tissue can reduce the sensitivity of the system by decreasing the effective ultrasound energy density at the beam interaction region. One may employ known phase aberration correcting methods to reduce such an effect. The practical value of these methods for USVA remains to be studied.

*Material evaluation*—Another field in which USVA can be potentially useful is material characterization, including mechanical parameter evaluation, imaging, and nondestructive testing of materials. The method described here can be used for detection and imaging flaws in materials. Also, one may use USVA to evaluate the mechanical frequency response of an object at low frequencies. In such case, we are interested in determining  $Q_{\Delta\omega}(x, y)$  versus frequency. We assume that the object is uniform within the projected area  $S$ . Then, the total radiation force on this object,  $F_{\Delta\omega}^-$ , can be calculated by integrating  $F_{\Delta\omega}(x, y)$  over  $S$ . Referring to Eqs. 21, one can show that, for  $\Delta\omega \ll \omega_0$ ,  $F_{\Delta\omega}^-$  is virtually independent of  $\Delta\omega$ . If  $H_{\Delta\omega}(l)$  is known and nonzero, then the function  $Q_{\Delta\omega}(x, y)$  can be estimated using Eq. 16 as  $Q_{\Delta\omega}(x, y) = \frac{P_{\Delta\omega}(x, y)}{F_{\Delta\omega}^- H_{\Delta\omega}(l)}$ . In practice,  $P_{\Delta\omega}(x, y)$  is obtained by sweeping  $\Delta\omega$  in the range of interest and recording the resulting acoustic emission [12].

## 7 ACKNOWLEDGMENTS

This work was supported in part by grant BC971878 from the Army Medical Research and

Materiel Command. The authors thank Randall R. Kinnick, Thomas Kinter, Elaine C. Quarve, and Julie M. Patterson for their support.

## 8 REFERENCES

1. Maynard, J. (Jan 1996) *Physics Today*. **49**(1), 26–31.
2. O'Donnell, M., Skovoroda, A. R., Shapo, B. M., Emelianov, S. Y. (1994) *IEEE Trans. Ultrason. Ferroelectr. Freq. Contr* **41**, 314–325.
3. Ophir, J., Cespedes, I., Ponnenkanti, H., Yazdi, Y., Li, X. (1991) *Ultrason. Imag.* **13**, 111–134.
4. Yamakoshi, Y., Sato, J., Sato T. (1990) *IEEE Trans. Ultrason. Ferroelectr. Freq. Contr.* **47**, 45–53.
5. Krouskop, T. A., Dougherty, D. R., Vinson, F. S. (1987) *J. Rehabil. Res. Dev.* **24**, 1–8.
6. Lerner, R. M., Huang, S. R., Parker, K. J. (1990) *Ultrasound Med. Biol.* **16**, 231–239.
7. Alam, S. K., Richards, D. W., Parker, K. J. (1994) *Ultrasound Med. Biol.* **20**, 751–758.
8. Gao, L., Parker, K. J., Lerner, R. M., and Levinson, S. F. (1996) *Ultrasound Med. Biol.* **22**(8), 959–977.
9. Muthupillai, R., Lomas. D. J. Rossman, P. J. Greenleaf, J. F., Manduca, A., Ehman, R. L. (Sept. 29, 1995) *Science* **269**, 1854–1857.
10. Sugimoto, T., Ueha, S. Itoh, K. (1990) *IEEE Ultrason. Symp. Proc.* 1377–1380.
11. Sarvazyan, A. P., Rudenko, O. V., Swanson, S. D., Fowlkes, J. B., Emelianov, S. Y. (1998) *Ultrasound in Med. Biol.* **24**, 1419–1435.
12. Fatemi, M., Greenleaf, J. F. (April 3, 1998) *Science* **280**, 82–85.
13. Beyer, R. T. (April 1978) *J. Acoust. Soc. Am.* **63**(4), 1025–1030.
14. Westervelt, P. J. (May 1951) *J. Acoust. Soc. Am.* **23**(4), 312–315.

15. Greenspan, M., Breckenridge, F. R., Tschiegg, C. E. (April, 1978) *J. Acoust Soc. Am.* 63(4), 1031–1038.
16. Morse and Ingard (1968) in *Theoretical Acoustics* (McGraw Hill, New York).
17. Morse, P. M. (1981) in *Vibration and Sound*, 3rd edition (The Acoustical Society of America).
18. Kino, G. S. (1987) in *Acoustics Waves: Devices, Imaging, and Analog Signal Processing*. (Prentice-Hall Signal Processing Series, Englewood Cliffs, NJ).

## 9 LEGENDS

Figure 1 Principle of ultrasound-stimulated vibro-acoustography.

Figure 2 Ultrasound-stimulated vibro-acoustography system. The confocal ultrasound annular array transducer with two elements is shown on the left.

Figure 3 Acoustic emission field intensity versus the combined ultrasound intensity.

Figure 4 USVA images of a 380  $\mu\text{m}$  glass bead: (A) in-phase, (B) quadrature, (C) phase, and (D) magnitude. The phase in (C) ranges from  $-\pi$  radians (black regions) to  $+\pi$  radians (white regions), and it was normalized to be zero at the center of the glass bead. (Modified with permission from [12]. Copyright 1998 American Association for the Advancement of Sciences.)

Figure 5 The theoretical PSF profile of the USVA system according to Eq. 24 and the glass bead in-phase image profile (Fig. 4a) obtained from the experiment.

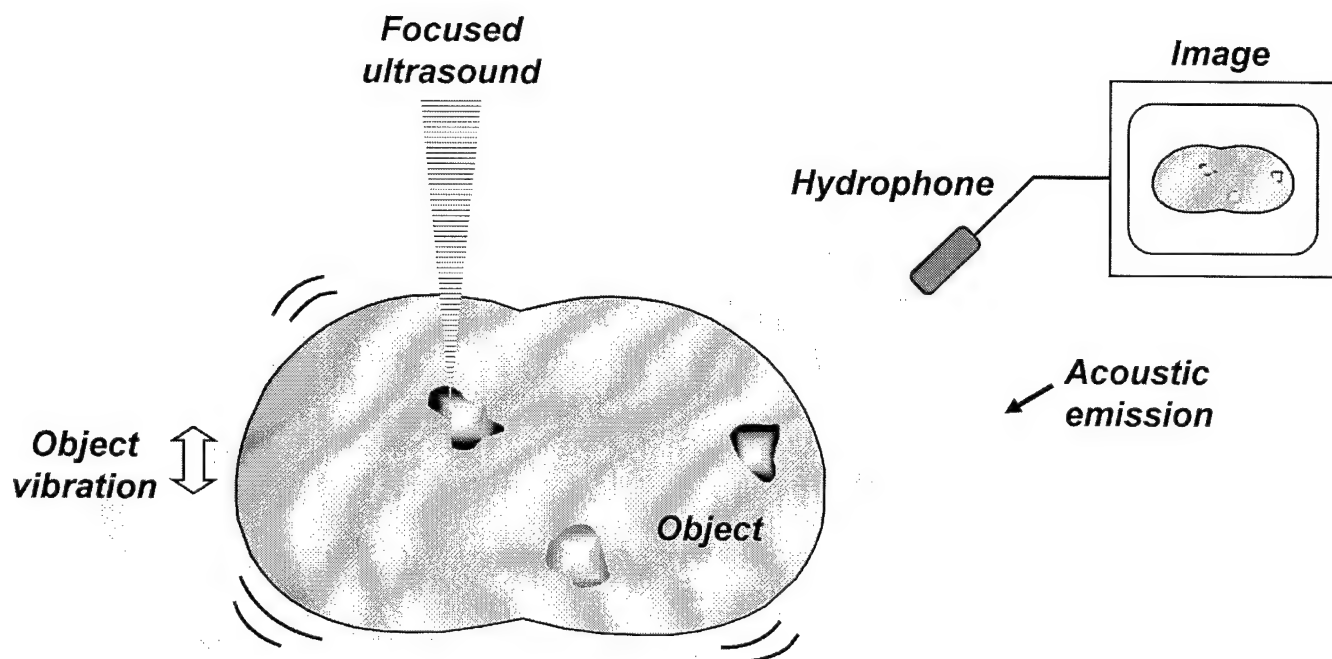


Fig. 1

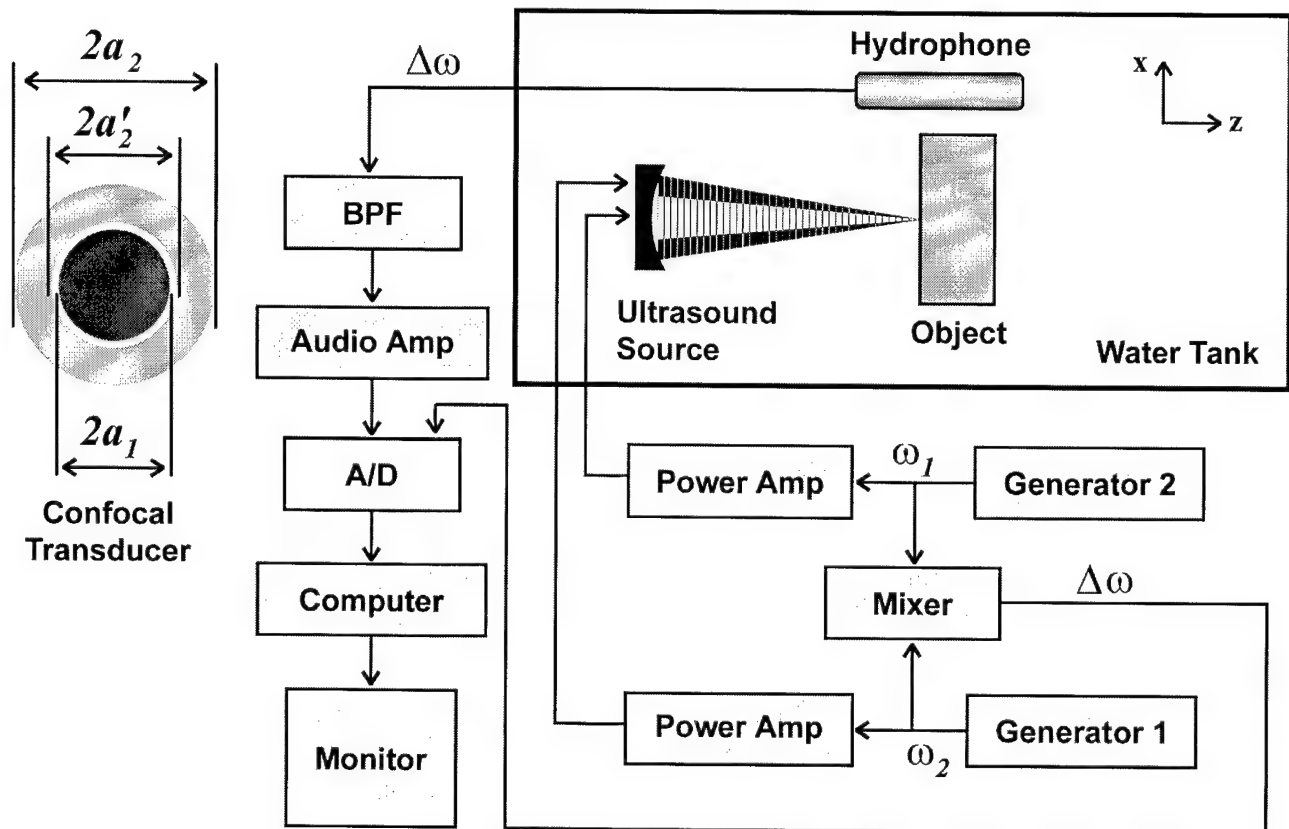


Fig. 2



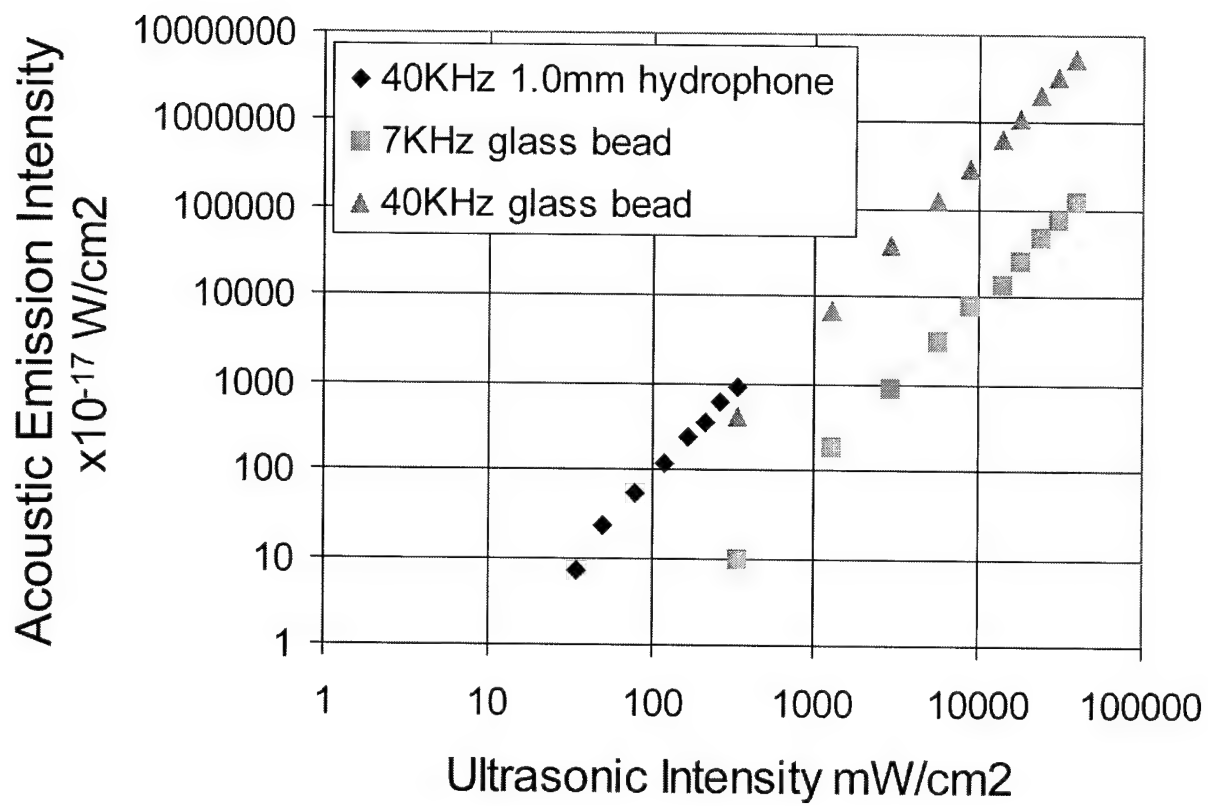


Fig. 3

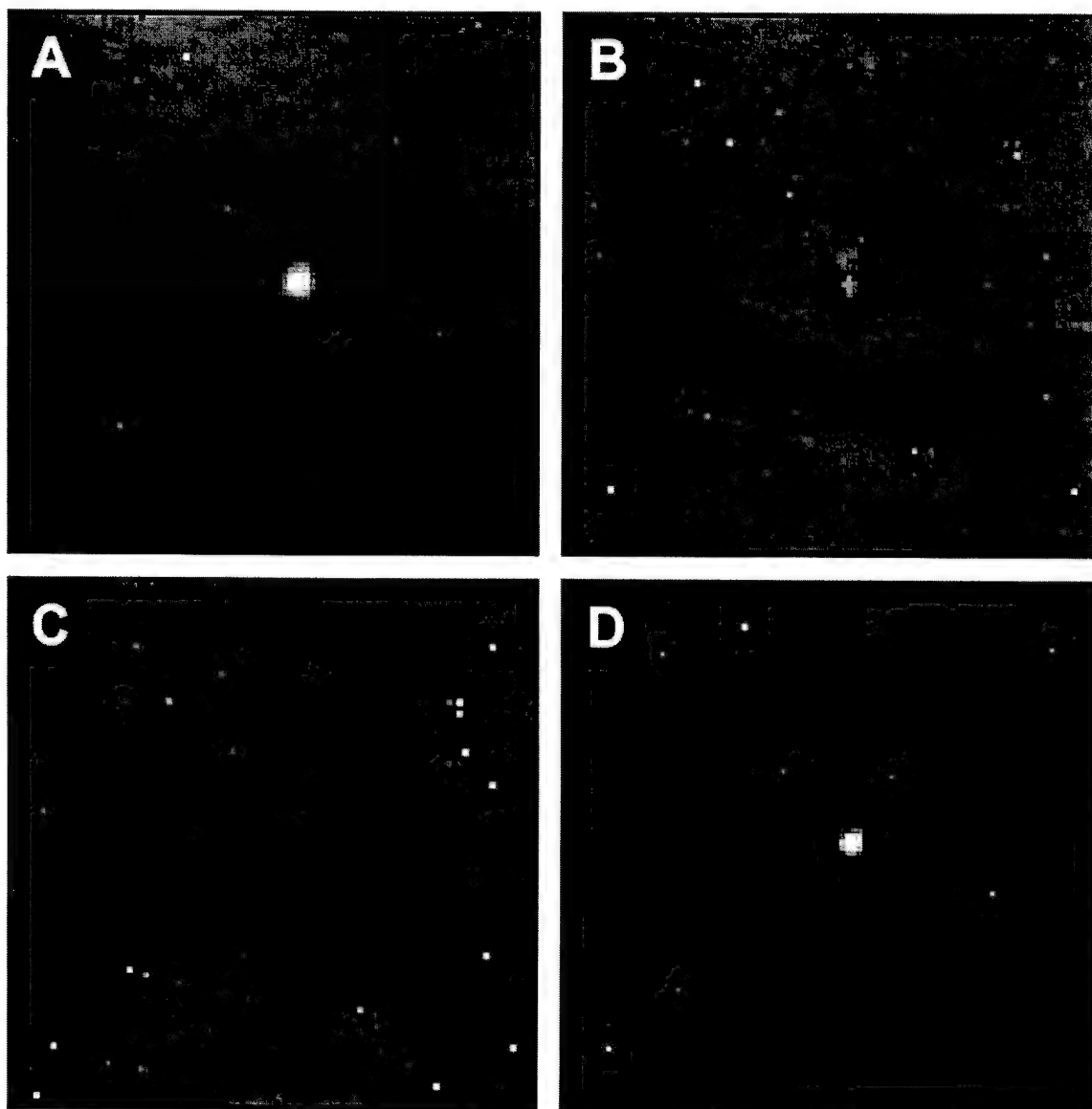


Fig. 4

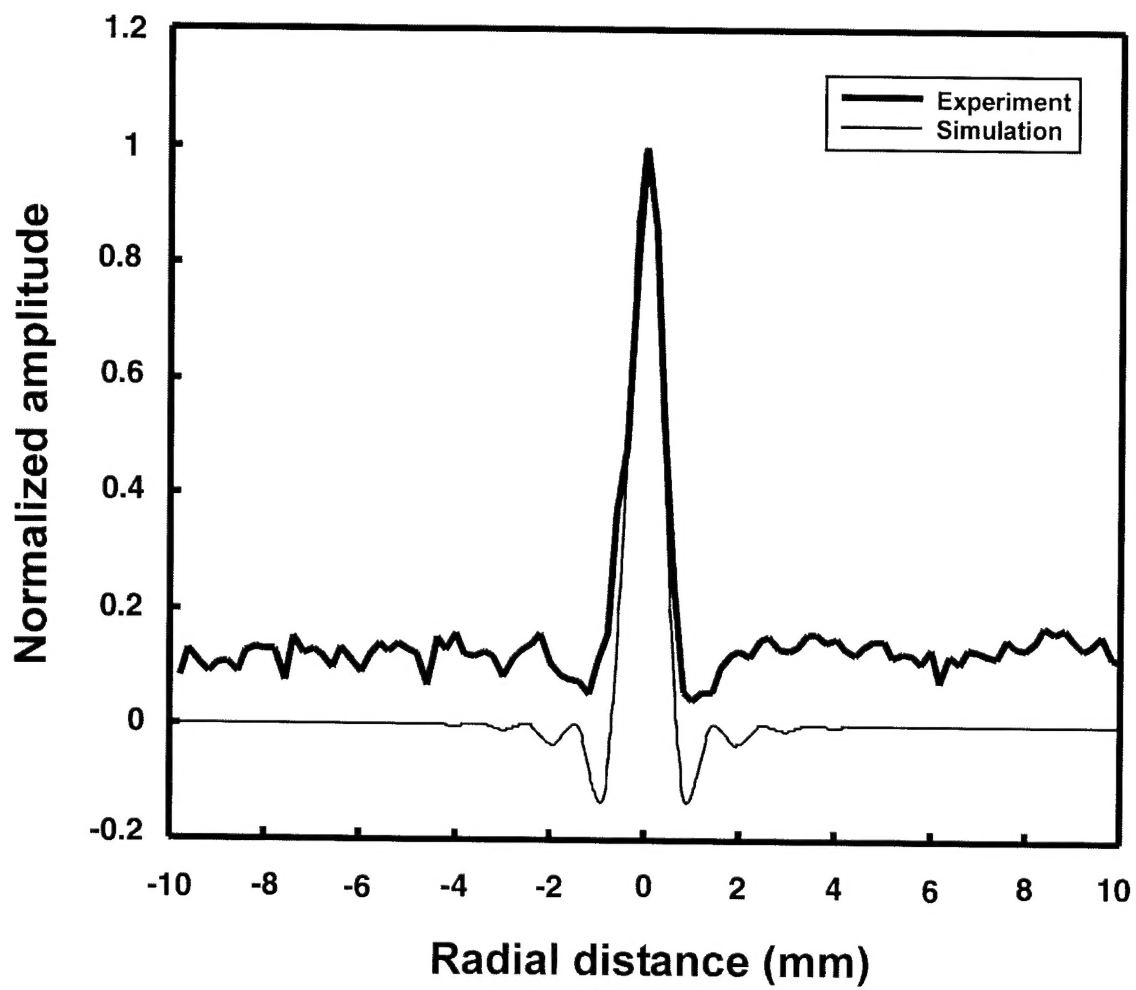


Fig. 5

ABSTRACT FORM

ABSTRACT DEADLINE: March 31, 1998

Official Use only

**Acoustic Field Calculation in Ultrasound-Stimulated Vibro-Acoustography**

Mostafa Fatemi and James F. Greenleaf

Department of Physiology and Biophysics, Mayo Clinic and Foundation, Rochester, MN 55905 USA

**Background:** In ultrasound-stimulated vibro-acoustography, two ultrasound beams are used to produce oscillating radiation force on the object under test. The resulting acoustic field is used to image the object. Here we discuss the analytical relationships between the ultrasound pressure field and the resulting acoustic field (acoustic emission). These relationships, which involve object mechanical parameters, can be used to deduce object characteristics from the received acoustic field.

**Method:** The radiation force of two intersecting ultrasound beams on an object is calculated. Assuming linearity, object displacement due to this force and the resulting acoustic emission pressure field are calculated.

**Results:** It is shown that the acoustic pressure amplitude is proportional to input ultrasound power. Also, acoustic amplitude is a function of object mechanical parameters such as the stiffness, mass, and the area.

**Conclusion:** The ultrasound-stimulated acoustic emission field of an object is related to object mechanical parameters via a closed form relationship. This allows estimation of object parameters from remote measurements of the acoustic emission field.

Mostafa  
First Name  
Physiology and  
Biophysics  
Department

Fatemi  
Middle Initial  
Last Name  
Mayo Clinic and Foundation  
Institution

PhD  
Degree

200 First Street Southwest  
Address

Rochester, MN  
City/State

USA  
Country

55905  
Postal Code

507 284-0608  
Telephone

507 284-1632  
Fax

fatemi.mostafa@mayo.edu  
E-Mail

## **Potential Applications of Ultrasound-Stimulated Vibro-Acoustography in Medical Diagnosis and material Characterization**

Mostafa Fatemi and James F. Greenleaf  
Ultrasound Research, Department of Physiology and Biophysics  
Mayo Clinic and Foundation  
Rochester, MN 55905

Elastic features of tissue are known to be highly correlated with tissue state and with some disease processes. Elastic constants are linked to numerous material properties, and hence, are valuable in nondestructive evaluation of materials. Recently, a new technique for imaging objects and evaluating their mechanical parameters was introduced by the authors [Science, (280):82-85, 1998]. This technique, ultrasound-stimulated vibro-acoustography (USVA), uses ultrasound to produce an oscillating, highly localized radiation force to vibrate the object at low frequencies. The resulting acoustic emission is a function of the local ultrasonic properties, which are measured by the conventional ultrasound, and are also a function of mechanical parameters (such as the elastic constants). This method, therefore, emulates the simplicity and high resolution of the conventional ultrasound, while providing additional information on low frequency mechanical features of the object. In the medical field, this method can provide high resolution images of tissue elasticity. Estimation of elastic parameters, such as stiffness, are valuable in diagnosis, for instance, to detect the presence of calcification within arteries or breast. Remote and nondestructive evaluation of viscosity, resonant frequency, and dynamic Young's modulus are potential applications of USVA in material science. Experimental results demonstrating various applications will be presented.

ICTCA'99 Fourth International Conference on Theoretical and Computational Acoustics,  
Trieste, Italy, May 10–14, 1999 (Invited, 9/29/98)

### **Beam Forming for Ultrasound-Stimulated Vibro-Asoustography**

Mostafa Fatemi and James F. Greenleaf

Ultrasound Research, Department of Physiology and Biophysics

Mayo Clinic and Foundation

Rochester, MN 55905

Ultrasound-Stimulated Vibro-Asoustography (USVA) is a recently developed method that utilizes ultrasound energy to evaluate the low-frequency mechanical parameters of an object [Science (280):82–85, 1998]. The novelty in this method results from combining the benefits of ultrasound with those of low-frequency elastic waves. This method takes advantage of the radiation force phenomenon to directly convert ultrasound energy to low frequency elastic waves in the object. Hence, the object response, in general, is a function of both the elastic parameters and ultrasonic characteristics of the object. The low frequency features of the object is of particular interest in many applications, including tissue imaging and characterization, and material science. Elastic parameters such as object stiffness, which are not available from the conventional ultrasonic methods, are valuable in medical field, for example to delineate hard deposits of calcifications in arteries from the surrounding soft tissue.

The principles used for ultrasound beam forming in USVA is fundamentally different from those for the conventional ultrasound imaging methods. The reason is that in USVA the ultrasound field is designed to interact nonlinearly with the object whereas in the conventional ultrasound they interact linearly.

In this paper, we describe USVA beam forming design methods, and present three beam forming configurations, including single, dual cross-beam (x-focal), and confocal beams. In the latter two configurations, the two ultrasound sources are driven at different frequencies. The acoustic field pressure and the resulting radiation stress on an elementary object are calculated. Analytical and simulation results indicate that the pressure and stress fields produced by the x-focal and confocal beams are circularly asymmetric and symmetric, respectively. The stress field in the confocal case is distributed according to the product of two Bessel functions of the first kind. Simulation results indicate that, given transducers with equal aperture size, the confocal beam produces the narrowest central lobe while the x-focal beam has the lowest sidelobe amplitude. Experimental results using focused 3.0 MHz transducers in a water tank are in agreement with the theoretical and simulation findings.